

Development of a New First-Level Trigger for Isolated Muons at the ATLAS experiment

by

Rubén Piles Delgado

Bachelorarbeit in Physik
vorgelegt dem Fachbereich Physik, Mathematik und Informatik (FB 08)
der Johannes Gutenberg-Universität Mainz
am 4. August 2025

1. Gutachter: Prof. Dr. Volker Büscher
2. Gutachter: Prof. Dr. Stefan Tapprogge

Hiermit erkläre ich, dass ich die vorliegende Arbeit selbstständig verfasst und keine anderen als die angegebenen Quellen und Hilfsmittel (dazu zählen auch KI-basierte Anwendungen oder Werkzeuge) benutzt habe. Sämtliche wörtlichen oder sinngemäßen Übernahmen und Zitate sind kenntlich gemacht und nachgewiesen. Ich versichere, dass ich keine Hilfsmittel verwendet habe, deren Nutzung die Prüferin oder der Prüfer explizit ausgeschlossen hat.

Im Anhang A.2 („Nutzung KI-Tools“) habe ich die verwendeten KI-Tools dokumentiert.

Mit Abgabe der vorliegenden Leistung übernehme ich die Verantwortung für das eingereichte Gesamtprodukt. Ich verantworte damit auch jegliche KI-generierten Inhalte, die ich in meine Arbeit übernommen habe. Die Richtigkeit übernommener (KI-generierter) Aussagen und Inhalte habe ich nach bestem Wissen und Gewissen geprüft.

Ich habe die Arbeit nicht zum Erwerb eines anderen Leistungsnachweises in gleicher oder ähnlicher Form eingereicht.

Mir ist bekannt, dass ein Verstoß gegen die genannten Punkte prüfungsrechtliche Konsequenzen hat und insbesondere dazu führen kann, dass die Studien- und Prüfungsleistung als mit „nicht bestanden“ bewertet wird. Die Einschreibung kann für bis zu zwei Jahre widerrufen werden, wenn Studierende zweimal oder häufiger bei Prüfungsleistungen täuschen (§ 69 Abs. 4 und 5 HochSchG).

Mainz, den 04.August.2025, Rubén Piles Delgado.

Rubén Piles Delgado
Institut für Physik
Staudingerweg 7
Johannes Gutenberg-Universität D-55099 Mainz
`rpilesde@students.uni-mainz.de`

Table of contents

1. Introduction and Motivation	1
2. Theoretical Background	3
2.1. The Standard Model of particle physics	3
2.1.1. The Strong Interaction	4
2.1.2. Electromagnetic and Weak Interactions	4
2.1.2.1. The Electromagnetic Interaction	4
2.1.2.2. The Weak Interaction	4
2.2. Particle Accelerators and Detectors	5
2.2.1. LHC Accelerator	5
2.2.2. ATLAS Detector	6
2.2.3. Coordinate System and Variables	7
2.3. ATLAS Trigger and Data Acquisition System	7
2.3.1. Level-1 Trigger	8
2.3.1.1. L1Calo	8
2.3.1.2. L1Muon	9
2.3.1.3. Central Trigger Processor (CTP)	10
2.3.2. High-Level Trigger (HLT)	10
3. Methodology and Results	11
3.1. Samples and Pre-selections	12
3.1.1. Prompt muons from $Z \rightarrow \mu^- \mu^+$ sample	12
3.1.2. Non-prompt muons from ZeroBias sample	14
3.2. Muon Isolation	17
3.2.1. Calorimeter Noise Cuts	18
3.2.2. Isolation ratios	20
3.3. ROC curve and Optimization	21
3.3.1. Receiver Operating Characteristic Curves	21
3.3.2. Isolation energy - p_T relationship	22
3.3.3. Noise cuts dependency	23
3.3.4. TopoEtCone heatmaps	24
3.3.5. Two-variable optimization	27
4. Summary and Outlook	29
4.1. Summary and Conclusions	29
4.2. Future work and improvements	29

Table of contents

A. Appendix	31
A.1. Tables and References	31
A.1.1. Invariant mass formulas [18]	31
A.1.2. Calorimeter Noise Cuts	31
A.1.3. Additional isolation plots	32
A.1.4. Additional two-variable optimization plots	37
A.2. Use of AI tools	38
A.3. Acknowledgements	38

1. Introduction and Motivation

“Deep is the abyss that is spanned by Durin’s Bridge, and none has measured it,” said Gimli.

“Yet it has a bottom, beyond light and knowledge,” said Gandalf.

—J.R.R. Tolkien, The Two Towers

The Standard Model of Particle Physics (SM) is one of the most complete, precise, and well-tested scientific theories ever developed by humankind. It provides scientists with a rich and detailed physical model to predict and explain many fundamental aspects of nature, such as the smallest “building blocks” of matter and how they interact with each other in the most basic ways.

Since its development during the 20th century, countless experiments have been conducted to test the theory and gain a better understanding of its strengths and weaknesses. These experiments have provided researchers with some of the most precise measurements ever made (e.g., the magnetic moment of the electron, with a relative uncertainty of 1.8×10^{-13} [1]), but they have also uncovered certain flaws in the theory, which is now considered incomplete (e.g., the lack of an explanation for the neutrino masses or the absence of dark matter particles).

Consequently, scientists are looking into more sophisticated theories, known as Beyond the Standard Model theories (BSM), that aim to fill the gaps left by the SM and expand our knowledge of fundamental physics.

In this context, particle accelerators have proven to be excellent tools, as they allow physicists to perform systematic and controlled measurements of particle properties. The largest particle accelerator in the world is currently the Large Hadron Collider (LHC) built by the European Organization for Nuclear Research (CERN) near Geneva, Switzerland. Its construction began in 1998 and took over ten years to complete, involving the work of thousands of professionals and institutions from around the world [2].

Since its construction, the LHC has contributed to many ground-breaking achievements, among them the discovery of the long-predicted Higgs boson by the CMS [3] and ATLAS [4] experiments in 2012.

ATLAS (short for *A Toroidal LHC ApparatuS*) is among the most complex

1. Introduction and Motivation

particle detectors ever built, designed to measure and record the properties of particles coming from collisions produced by the LHC. When it is operating, massive amounts of collision data are recorded every second [5] and it becomes impossible to store everything. Because of this, scientists have developed a variety of techniques to filter and select events considered the most “interesting” for their current research goals —the Trigger and Data Acquisition System (TDAQ). Thanks to this system, the recorded event rate is reduced from around 40 MHz (one collision every 25 ns) to approximately 3 kHz[15].

Upgrades to the LHC are currently taking place to increase its luminosity by a factor of five above the original design value. It is expected to be operative by the end of the 2020s under the name of High-Luminosity LHC (HL-LHC) [7]. The total amount of data collected is expected to go up from $\sim 400 \text{ fb}^{-1}$, corresponding to Run 2 and 3, to more than 3000 fb^{-1} ¹. In this context, it is essential to continue improving the TDAQ system so it can handle the increasing number of collision data produced.

This thesis focuses on optimizing an aspect of the Level-1 Trigger System (L1 Trigger), one of the key components of the TDAQ system. It aims to improve the methodology used to distinguish leptons produced directly in the initial high-energy proton-proton collisions —known as *prompt leptons*— from those produced in secondary decays —called *non-prompt leptons*.

¹At the LHC, data is expressed in inverse femtobarns (fb^{-1}), a measure of integrated luminosity that reflects the total number of recorded collisions

2. Theoretical Background

In the following chapter, a summary of relevant theoretical aspects is given based on [22].

2.1. The Standard Model of particle physics

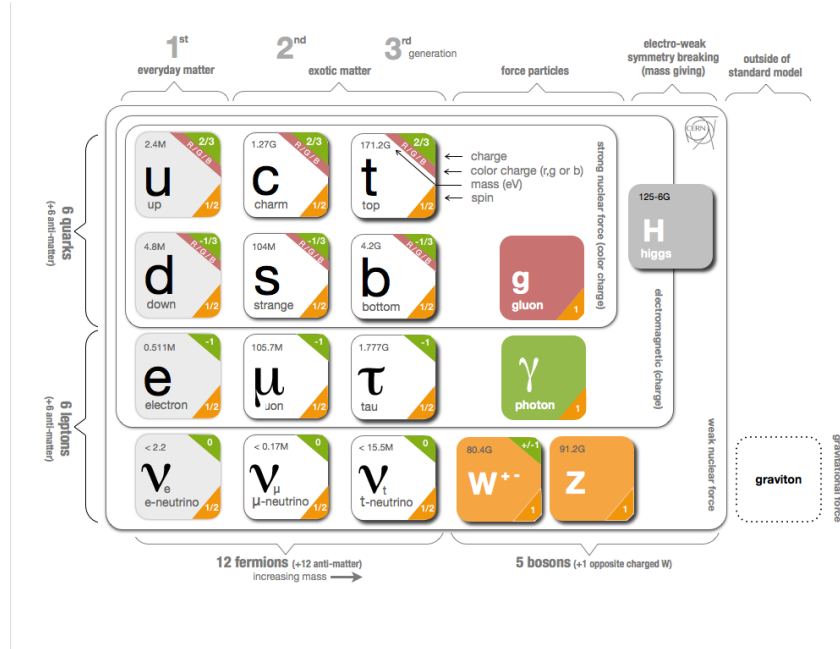


Figure 2.1.: Standard Model elementary particles [8]

It is widely accepted in modern physics that all physical interactions can ultimately be classified into four fundamental categories: strong, weak, electromagnetic and gravitational interactions. Each of these fundamental interactions is mediated by the exchange of particles —known as force carriers— except for gravity, for which a mediating particle, the graviton, has not yet been experimentally observed. These interactions possess different characteristics in terms of relative strength, ranges, associated conservation laws, and particles affected.

The Standard Model of particle physics is a quantum field theory that describes three of the four fundamental interactions, excluding gravity. It integrates all known elementary particles, believed to be the smallest indivisible constituents from which

2. Theoretical Background

all ordinary matter is formed. An overview of the fundamental particles is shown in Figure 2.1.

2.1.1. The Strong Interaction

According to the SM, *quarks* are elementary particles that exist in six different types, commonly known as *flavors*. Since quarks possess color charge, they take part in strong interactions. Quarks can also interact electromagnetically and weakly. Depending on how quarks combine, two different kinds of particles can be distinguished: baryons, which are made of three quarks, and mesons, which consist of one quark and one antiquark.

Gluons serve as the force carriers of the strong interaction. Gluon exchange generates a powerful binding force between quarks that increases with distance—similar to a spring connecting quarks—, forcing them to combine into relatively stable configurations (hadrons).

2.1.2. Electromagnetic and Weak Interactions

Leptons are particles that do not carry color charge and, consequently, are not involved in strong interactions. The Standard Model predicts three electrically charged leptons, with charge ± 1 (electron, muon, and tau), and three electrically neutral neutrinos (electron neutrino, muon neutrino, and tau neutrino). Neutrinos interact only via the weak interaction, while the charged leptons also participate in electromagnetic interactions.

Compared to the abundance of processes mediated by the strong interaction, those involving electroweak interactions are extremely rare 2.4. Since leptons can only be produced through electroweak interactions, they are of significant interest in current physics research.

2.1.2.1. The Electromagnetic Interaction

The working principles of this interaction are described by a theory known as Quantum Electrodynamics (QED). Photons (γ) act as the force carriers of this interaction. Unlike the strong and weak interactions, which are confined to subatomic distances, the electromagnetic interaction has infinite range.

2.1.2.2. The Weak Interaction

The weak interaction involves three force carriers: the Z , W^+ , and W^- gauge bosons. Prompt leptons can be produced in these weak processes. For this study, a particularly relevant example is the decay of a Z boson into a muon-antimuon pair ($Z \rightarrow \mu^- \mu^+$).

2.2. Particle Accelerators and Detectors

Particle accelerators are instruments with a wide range of applications, including scientific research, industrial processes, and medical treatments. Using electric fields, particle beams can be accelerated from rest to relativistic speeds. Since many particle physics experiments require high-energy beams, these instruments are extensively used in this field.

Particle detectors are an essential tool for measuring the outcomes of particle collisions and interactions. Using different techniques, such as calorimetry, spectrometry and particle tracking [9], physicists are able to determine the properties of the resulting particles.

2.2.1. LHC Accelerator

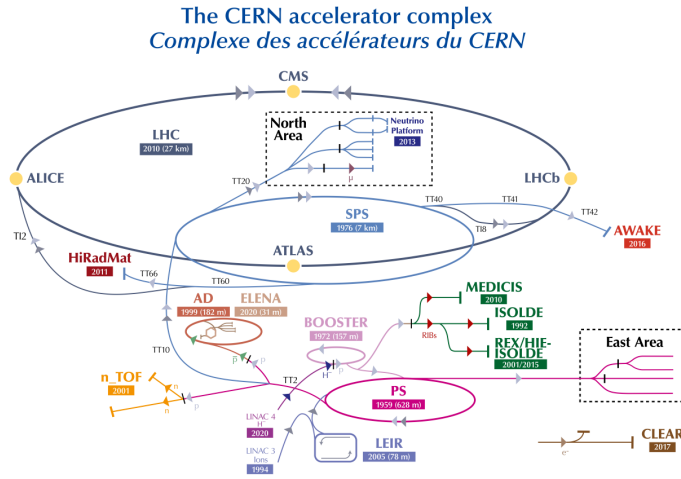


Figure 2.2.: Scheme of the CERN accelerator complex[11]

The Large Hadron Collider (LHC) is the world's largest and highest-energy particle accelerator. Here, two proton beams are accelerated in opposite directions up to an energy of 6.8 TeV per proton and collided symmetrically, resulting in a center of mass collision energy of approximately 13.6 TeV [10]. It is housed in a 26.7-kilometer-long circular tunnel, where beams reach their final energy after completing thousands of revolutions around it.

To achieve this threshold, protons are extracted from hydrogen gas and accelerated in a series of smaller accelerators before being injected to the LHC. A scheme of the complete accelerator complex is displayed in 2.3. Radio frequency cavities located at the ring generate oscillating electric fields that accelerate the beams forward every time they pass through. To maintain beams focused and in their

2. Theoretical Background

circular path, 1232 dipole and 392 quadrupole superconducting magnets, cooled down to 1.9 K, are employed.

The LHC circulates beams that are collided at four different interaction points, where the particle detectors —ALICE [23], CMS[24], LHCb[25] and ATLAS[9]— are located. These beams are structured into discrete bunches, with up to 2808 bunches per beam and a temporal spacing of approximately 25 ns between bunches.

2.2.2. ATLAS Detector

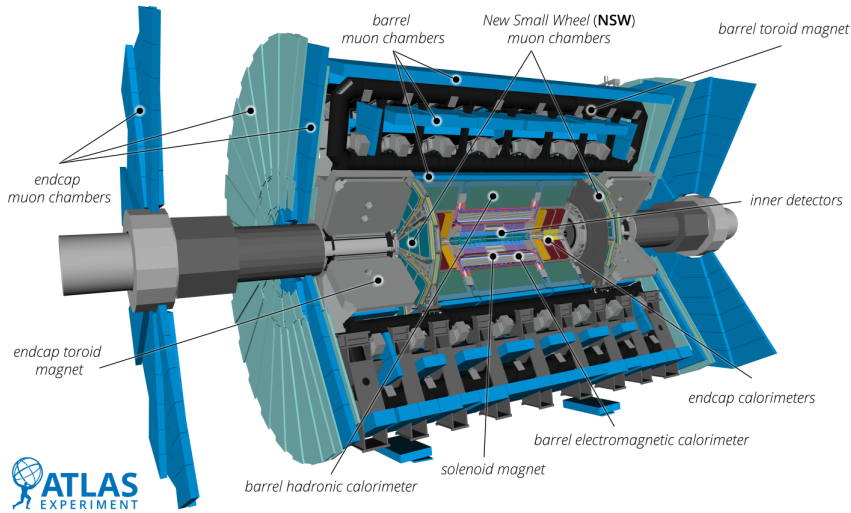


Figure 2.3.: Scheme of the ATLAS detector subsystems [12]

The ATLAS experiment[9] is the largest general-purpose, collider-based particle detector in the world. It is capable of recording a broad range of particle properties —such as energy, momentum, and charge— and reconstructing their trajectories. It is composed of three principal detecting subsystems, arranged in concentric layers around the central axis of the detector—Inner Detector, Calorimeter, and Muon Spectrometer. Proton-proton collisions occur at the center of the ATLAS detector, generating cascades of particles that propagate from the collision point in all directions, where they encounter the detection systems.

1. **Inner Detector:** Located inside a solenoid magnet, which generates a magnetic field of 2 T, the trajectories of charged particles are bent by the Lorentz force. The primary function of the Inner Detector is to track these particles and measure their charge and momentum based on the curvature radius and direction.
2. **Calorimeter:** By absorbing particles, the calorimeter measures their energy. The inner section, known as the electromagnetic calorimeter, is designed to mea-

2.3. ATLAS Trigger and Data Acquisition System

sure the energies of electrons and photons. Hadrons typically penetrate deeper into the detector and are measured by the outer section, called the hadronic calorimeter.

3. **Muon Spectrometer:** Due to their high mass and lack of strong interaction, muons often penetrate through the inner detector and calorimeter without being fully absorbed, which is why a dedicated muon spectrometer is needed. This subsystem consists of layers of gas-filled chambers that become ionized when a muon passes through. Combined with magnetic fields that bend their trajectories, the muon spectrometer allows for precise reconstruction of the muons' paths and momenta.

2.2.3. Coordinate System and Variables

In order to adapt to the experiment's requirements, a modified version of the spherical coordinates (r, ϕ, θ) and specific kinematic variables are used. Protons are composite particles made up of quarks and gluons (partons), each carrying a random fraction of the proton's total momentum, as described by parton distribution functions (PDFs) [20]. As a result, the exact momentum of a parton-parton collision along the beam axis (z axis) is unknown. However, the initial transverse momentum of the system is zero and is conserved after the collision. Consequently, the use of transverse momentum (p_T), instead of total momentum, enables for precise measurements and estimation of missing transverse energy [18]. Moreover, *pseudorapidity* (η) is used in place of the polar angle (θ), since it is approximately Lorentz-invariant under boosts on the z axis and well-suited for detector's geometry. It is defined as:

$$\eta \equiv -\ln \left[\tan \left(\frac{\theta}{2} \right) \right]$$

To represent the angular distance between two points in the ATLAS coordinate system, the quantity $\Delta R := \sqrt{\Delta\phi^2 + \Delta\eta^2}$, where $\Delta X = X_2 - X_1$, is defined. Additionally, the massless approximation ($E^2 = m^2c^4 + p^2c^2 \approx p^2c^2$) is often employed, since $p \gg m$ for many high-energy experiments.

2.3. ATLAS Trigger and Data Acquisition System

ATLAS is designed to observe millions of proton-proton collisions per second. As illustrated in Figure 2.4, the most common events have a much larger production cross section, making them far more frequent than the rarer events. Consequently, the data collected for these common events is already extensive.

Due to the impossibility of recording or storing all the data generated, which is estimated to produce a combined data volume exceeding 60 terabytes per second, attention is directed toward the rare events, which have a smaller production cross section but are of greater significance for current physics research. The ATLAS

2. Theoretical Background

Trigger, a two-level event selection system, is specifically designed to “decide” in real time whether an event contains interesting properties and should be stored for further analysis. Additional details can be found in [15].

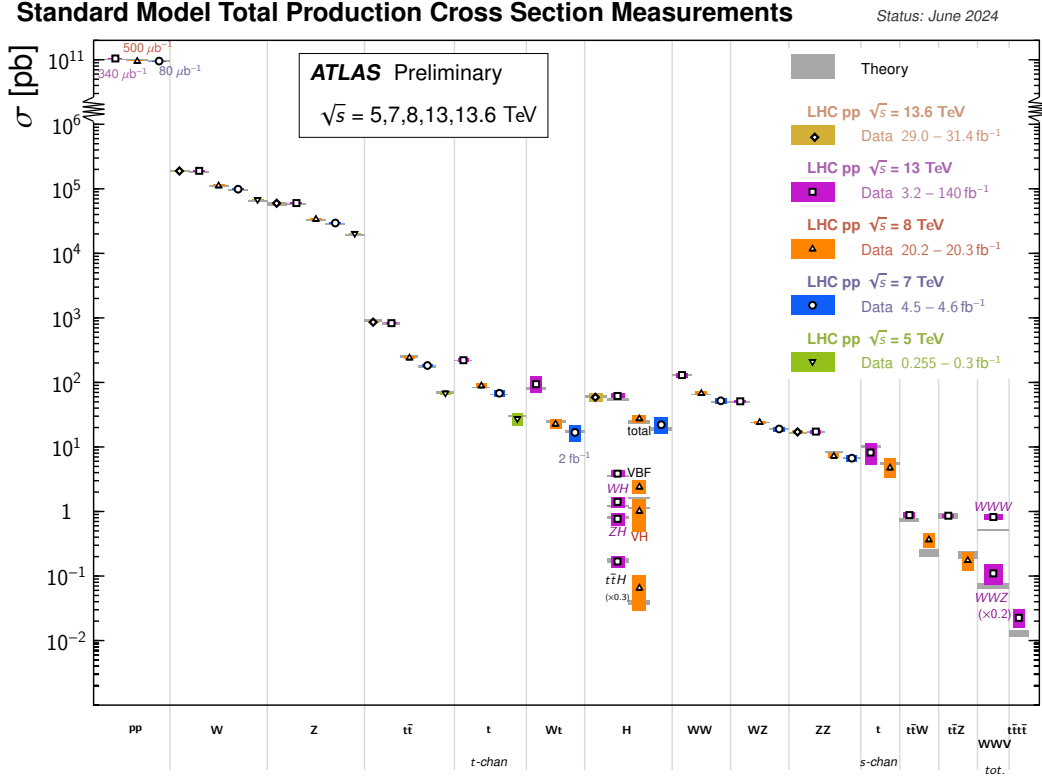


Figure 2.4.: Plot showing how some events are much more likely to happen than others, in terms of production cross section [19]

2.3.1. Level-1 Trigger

Using custom-made hardware, the Level-1 Trigger¹ uses data from dedicated calorimeter (L1Calo) and muon spectrometer (L1Muon) detectors to decide, in less than 2.5 μs , if an event should be analysed further or discarded. The initial collision rate is 40 MHz, but after the filtering process, only ~ 100 kHz are retained. A scheme of its components is shown at Figure 2.6.

2.3.1.1. L1Calo

L1Calo analyzes the energy values deposited in small areas of the calorimeter, known as *trigger towers*. The energy values are digitized and filtered at a rate of 40 MHz [16].

¹In the HL-LHC upgrade, it is planned that the Level-1 Trigger will be referred to as Level-0.

2.3. ATLAS Trigger and Data Acquisition System

There are different Feature Extractors (FEXes) in the L1Calo system, each designed to identify specific signatures and receive inputs with varying granularities depending on their purpose. These FEXes are specialized for tasks such as identifying jets, electrons, or taus.

The Jet Feature Extractor (jFEX) is a high-speed, FPGA²-based processor that forms part of the L1Calo system. It is designed to identify *jets*—streams of particles resulting from quark or gluon hadronization—and to compute global event quantities such as the total transverse energy. There are 7680 jFEX trigger towers, with a typical granularity of $\Delta\eta \times \Delta\phi = 0.1 \times 0.1$ in the central region, becoming coarser at higher η . Operating at the full LHC bunch crossing rate of 40 MHz, jFEX processes real-time calorimeter data to determine whether an event should be passed to the next stage of the trigger system.

2.3.1.2. L1Muon

Depending on their momentum, muons can penetrate thick layers of material with minimal interaction, allowing them to pass through the calorimeter without being stopped, as shown in Figure 2.5. Because of this, a dedicated muon trigger is needed.

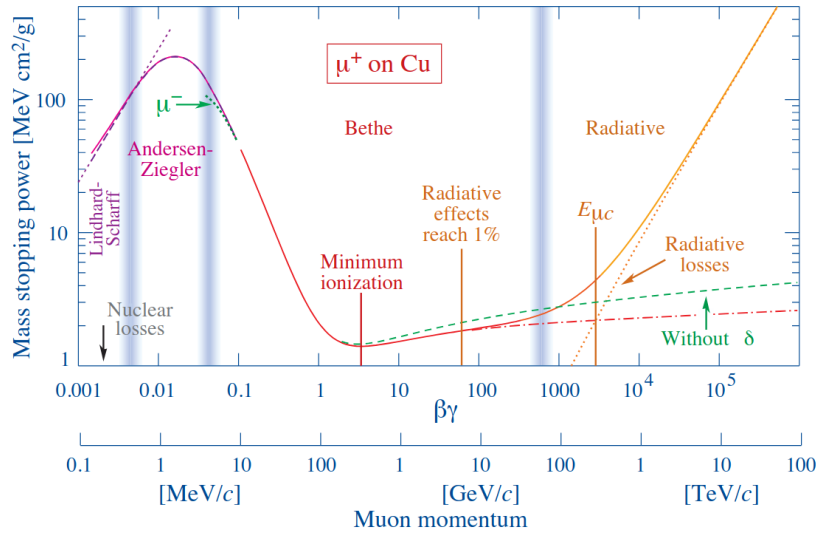


Figure 2.5.: The amount of energy lost by a muon per unit of length when penetrating a material depends on its momentum [21]

The L1Muon trigger identifies muons by searching for sequences of hits across multiple layers of muon spectrometer chambers, known as *stations*. For each station, predefined *coincidence windows*, corresponding to different muon p_T thresholds [15], are used to

²Abbreviation for Field-Programmable Gate Array

2. Theoretical Background

determine the range of downstream stations that a muon could reach starting from the interaction point based on its curvature in the magnetic field [16].

2.3.1.3. Central Trigger Processor (CTP)

Finally, inputs from L1Calo, L1Muon and other additional systems are fed to the CTP, where a final decision is made by combining all the available information [16].

2.3.2. High-Level Trigger (HLT)

The High-Level Trigger is a software-based tool that performs a deeper analysis of the data selected by the Level-1 trigger. Here, a physical reconstruction of the events is computed, using the full detector data. Finally, the refined collision data is stored at data centers around the world for future use, at an approximate rate of 3 kHz. [17]

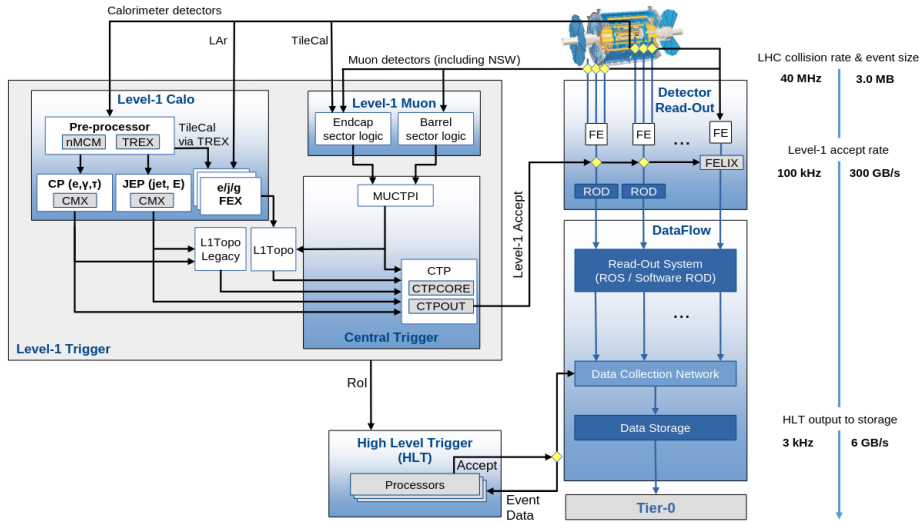


Figure 2.6.: Scheme of the ATLAS Trigger System [15]

3. Methodology and Results

The primary objective of this study is to present a proof-of-concept approach for enhancing the capabilities of the Level-1 Trigger system, specifically in distinguishing muons originated from the original $p - p$ collision (prompt muons) from those produced by secondary in-flight processes, such as hadron decays.

To achieve this, calorimeter-based *isolation energies* for both prompt and non-prompt muons are computed. Muon isolation is a technique applied to collision data to distinguish prompt from non-prompt muons. The isolation procedure involves drawing hollow cones—with an inner and outer ΔR radius—around recorded muon impact points, as illustrated in 3.1. A measurement of the total calorimeter energy

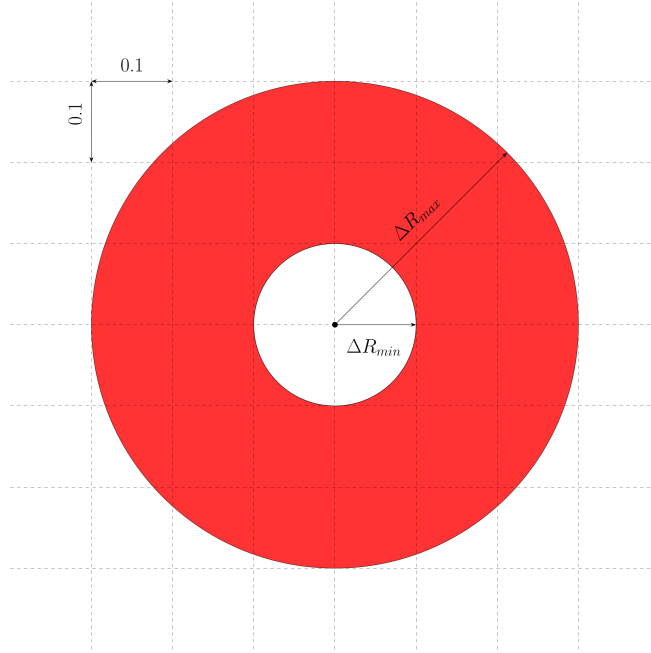


Figure 3.1.: Hollow cone with $[\Delta R_{min}, \Delta R_{max}] = [0.1, 0.3]$. The grid represents calorimeter towers with granularity $\Delta\eta \times \Delta\phi = 0.1 \times 0.1$.

located within the cone volume, often referred to as *isolation energy*, is obtained by summing the calorimeter energies registered by each of the trigger towers whose center is located inside the hollow cone's area.

This process allows for the discrimination between prompt and non-prompt

3. Methodology and Results

muons, since muons originating from secondary decays are typically surrounded by a *jet*. In contrast, prompt muons usually present less activity around them, as they are mainly produced by $Z \rightarrow \mu^- \mu^+$ or $W \rightarrow \mu \nu$ decays, which do not produce jets. As a result, one can expect differences in isolation energy that help distinguish between prompt and non-prompt muons.

3.1. Samples and Pre-selections

The analysis focuses on a dataset comprising both offline and online *objects* — particles reconstructed from raw collision data— recorded by ATLAS during Run 3. In this context, online data refers to information collected and processed in real time by the trigger system during data-taking, while offline data undergoes detailed and time-consuming reconstruction after data-taking.

Given that the muon triggers planned for Run 4 are expected to yield samples comparable to those obtained through current offline muon reconstruction, offline data is used in this study to emulate future trigger resolution.

The dataset consists of two distinct sources: a $Z \rightarrow \mu^- \mu^+$ sample, dominated by prompt muons, and a ZeroBias sample, enriched in non-prompt muons.

3.1.1. Prompt muons from $Z \rightarrow \mu^- \mu^+$ sample

$Z \rightarrow \mu^- \mu^+$ events are of interest because, by requiring the invariant mass of the muon pair to be close to the mass of the Z boson, a clear and distinguishable source of prompt muons is identified. To identify an event as $Z \rightarrow \mu^- \mu^+$ in ATLAS, several criteria must be satisfied.

First, the event must pass the muon trigger, ensuring a high probability of containing muons. The event must then have two muons: one with a transverse momentum of at least 25 GeV and another with at least 20 GeV. Both muons must pass a track-based isolation requirement to ensure they are isolated from other particles in the event. Finally, the invariant mass of the two muons must lie between 70 and 110 GeV, consistent with the mass of the Z boson.

Additional pre-selections have been applied to further increase the purity of the sample:

1. **Z peak selection:** As shown in Figure 3.2, the provided $Z \rightarrow \mu^- \mu^+$ events often contain more than two muons, which are considered as potential candidates for the Z boson decay. Since, by definition, only one pair of muons can result from the decay, the “best pair” is pre-selected by calculating the invariant mass of all possible muon pairs, using p_T , η , and ϕ , as detailed in A.1.1. For example, in an event with three muons (μ_1, μ_2, μ_3) , the possible pairs would be (μ_1, μ_2) ,

3.1. Samples and Pre-selections

(μ_2, μ_3) , and (μ_1, μ_3) . The pair whose invariant mass is closest to the Z boson mass ($\approx 91.2 \text{ GeV}$ [26]) is selected, since it is very likely to contain prompt muons. After this pre-selection, potential non-prompt muons have been filtered out and only events with two prompt muons remain, as shown in Figure 3.2.

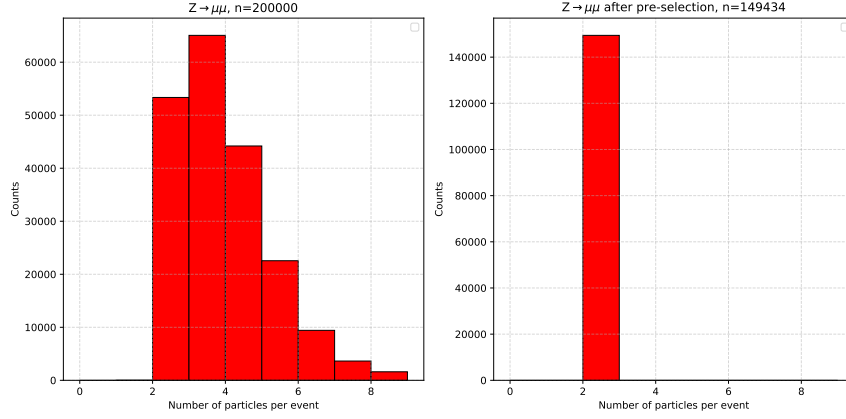


Figure 3.2.: Number of particles per event, before and after pre-selections

2. **High quality selection:** For the $Z \rightarrow \mu^- \mu^+$ sample, only high-quality muons, labeled as “Quality= 0”, were used. The quality value quantifies the reliability of the reconstructed muon, taking into account factors such as the number of hits in the tracking detectors and the consistency between different detector subsystems [27]. Muons with Quality = 0 meet the highest reconstruction standards, resulting in a sample with a high fraction of prompt muons. As shown in Figure 3.3, these muons produce a sharper peak around the Z boson mass.

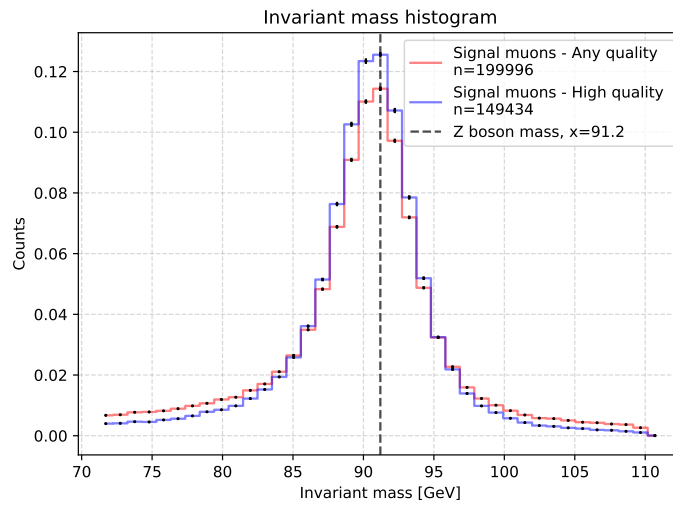


Figure 3.3.: Invariant mass before and after high quality pre-selection

3. Methodology and Results

3.1.2. Non-prompt muons from ZeroBias sample

The ZeroBias sample consists of events recorded by the ZeroBias trigger, which selects random events that are not subject to specific selection criteria. These events are unbiased and not influenced by any particular process. Instead, the contents of ZeroBias events reflect the cross-section of the underlying processes. As a result, the sample predominantly contains non-prompt muons, which are more common, and provides an unbiased reference for studying background processes. Additionally, it is useful for estimating the impact of the isolation selection on the trigger rate, as it offers a uniform representation of the detector's performance across different types of events.

Moreover, the following pre-selections were applied to the ZeroBias sample:

1. **Online-Offline matching:** The majority of offline muons in the ZeroBias sample are reconstructed from calorimeter energy deposits. However, this study focuses exclusively on muons detected by the muon system. Since online muon reconstruction is based solely on the muon spectrometer, offline muons in the Zero Bias sample are selected only if they are spatially close to an online muon. This is quantified by the distance ΔR between an offline muon and any online muon, which must be smaller than a specified threshold. In this analysis, this threshold is set to 0.4.
2. **Low- p_T cut:** Since low- p_T muons are rejected by trigger, the $Z \rightarrow \mu^- \mu^+$ sample contains very few low- p_T muons —especially below the 14 GeV threshold— compared to the Zero Bias sample, as illustrated in 3.4. To ensure comparable

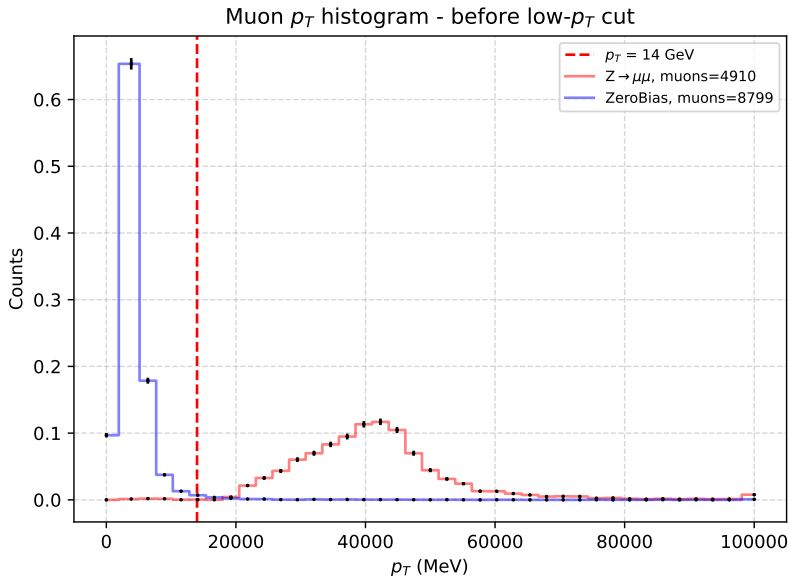


Figure 3.4.: Muon p_T spectra before low- p_T cut.

3.1. Samples and Pre-selections

p_T spectra between the signal and background samples, a 14 GeV low- p_T cut has been applied to the ZeroBias dataset. As a result, muons with transverse momentum below 14 GeV have been removed from the background sample. However, it is important to note that the p_T spectra of the signal and background samples remain quite different after the pre-selections. This discrepancy will impose limitations on the methods used, as discussed in 3.2.2.

After applying the pre-selections, a signal sample—expected to contain a high fraction of prompt muons—is derived from the original $Z \rightarrow \mu^- \mu^+$ dataset, while a background sample, dominated by non-prompt muons, is obtained from the original Zero Bias dataset. Figures 3.5, 3.6 and 3.7 display histograms of p_T , η , and ϕ , after pre-selections.

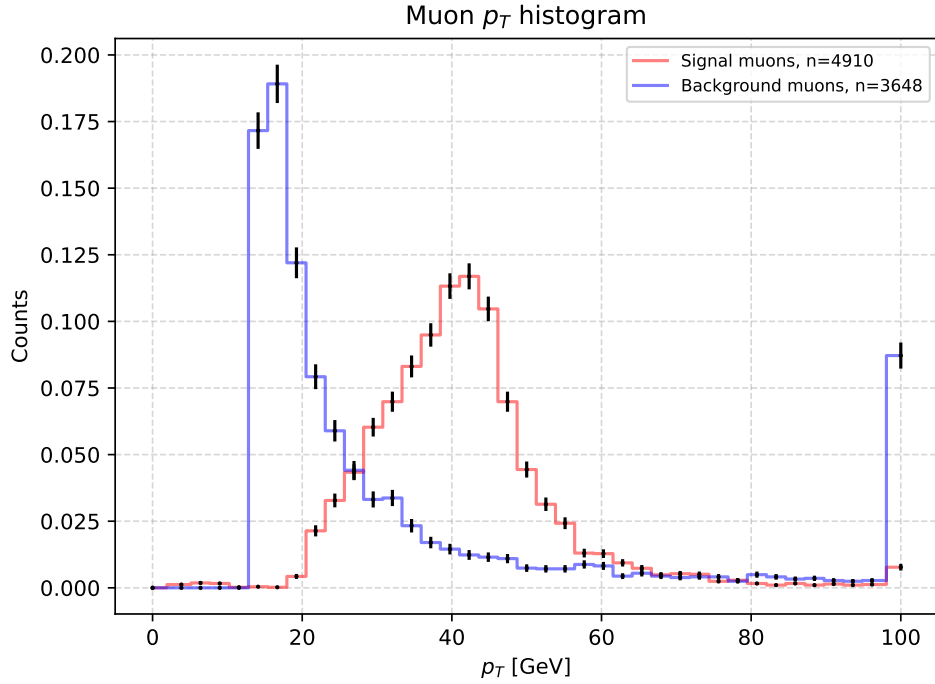


Figure 3.5.: Muon p_T spectra after pre-selections

3. Methodology and Results

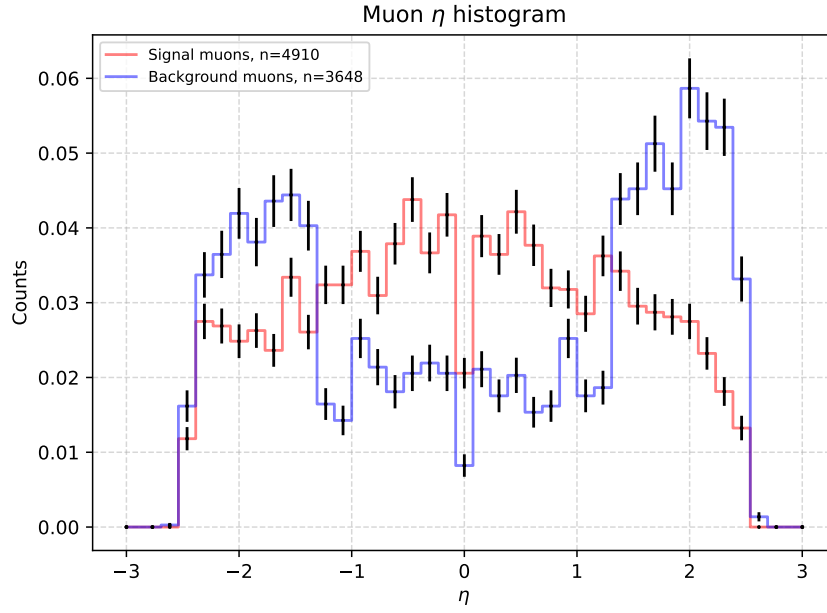


Figure 3.6.: Muon η histogram after pre-selections

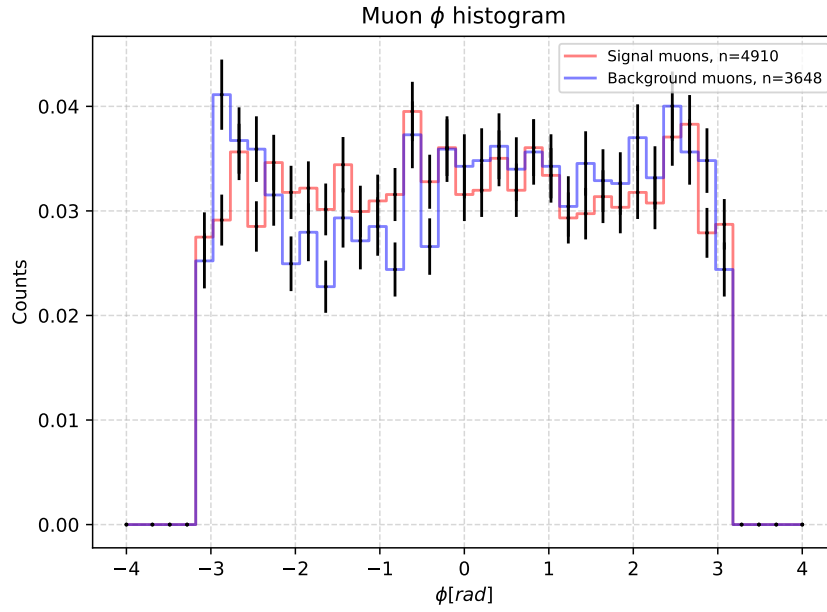


Figure 3.7.: Muon ϕ histogram after pre-selections

3.2. Muon Isolation

Muon isolation energies were computed to distinguish between prompt and non-prompt muons. As shown in Figures 3.8 and 3.9, the results depend on the choice of the ΔR cone. Additional plots can be found in A.1.3.

The dependence of isolation energies on ΔR can be explained by the fact that increasing the outer radius includes more calorimeter towers in the calculation, leading to higher isolation energy values. For the inner radius, introducing a hole in the center of the cone effectively excludes most of the muon's energy, resulting in a reduction in the isolation energy. Observing the difference in position of the vertical dashed red line—which indicates the point in the x-axis where 95% of the signal distribution is located to the left—between 3.8 and 3.9, this leads to a typical energy reduction of ~ 2.5 GeV, corresponding to the energy deposited by muons in the calorimeter.

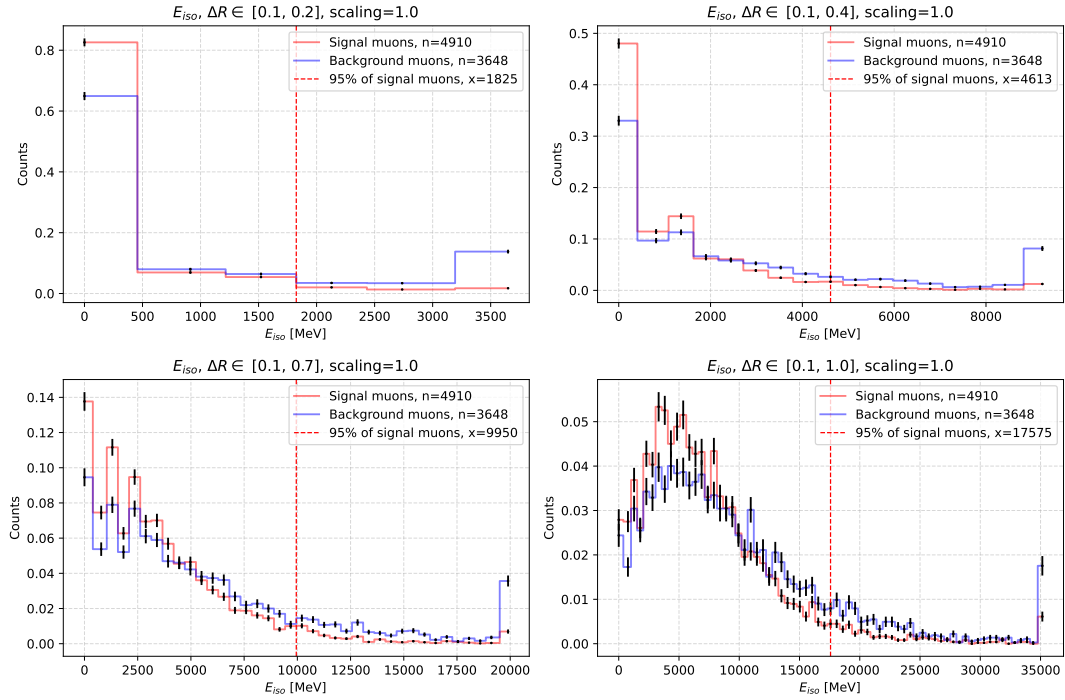


Figure 3.8.: Isolation energy histograms with different ΔR hollow cones

3. Methodology and Results

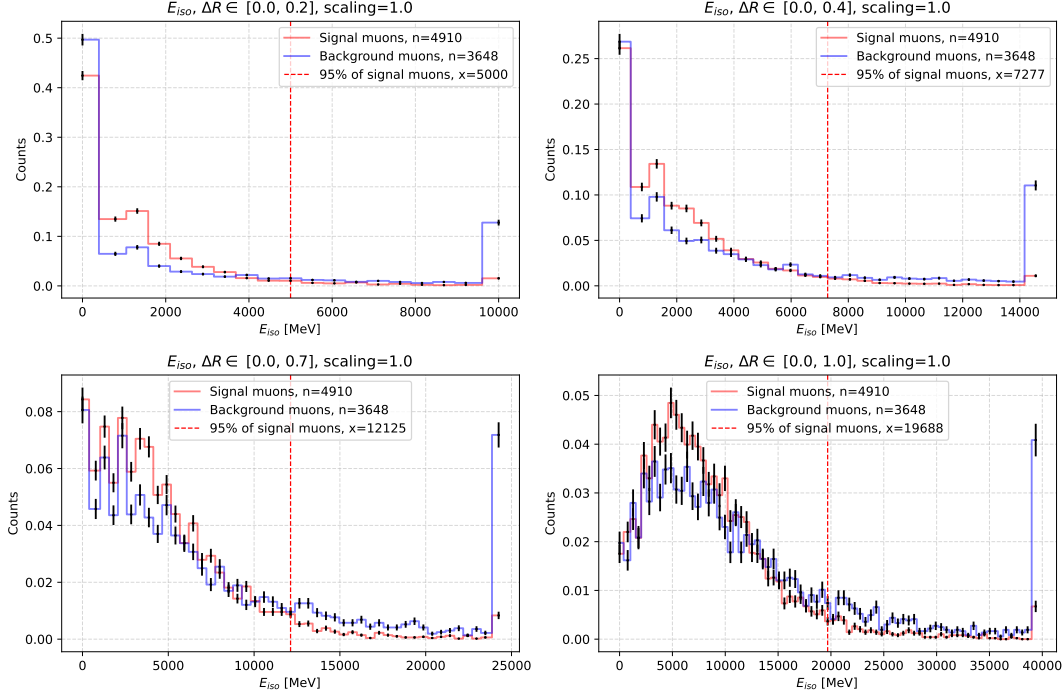


Figure 3.9.: Isolation energy histograms with different ΔR solid cones

3.2.1. Calorimeter Noise Cuts

Undesired energies registered in the calorimeter can blur the ability to discriminate between prompt and non-prompt muons. These unwanted energies often arise from detector noise —caused by electronic readout or sensor imperfections— or *pile-up* —additional proton-proton collisions that occur in the same bunch crossing, creating extra particles that overlap with the signal from the primary interaction.

To mitigate these effects, energy noise cuts are applied based on the type and position of the calorimeter towers. These cuts impose a minimum energy threshold for each tower, and any tower with energy below this threshold is considered *noise* and set to zero.

The specific noise cuts applied are detailed in A.1.2. Figures 3.10, 3.11 illustrate the impact of varying the noise cut thresholds on the isolation energies.

3.2. Muon Isolation

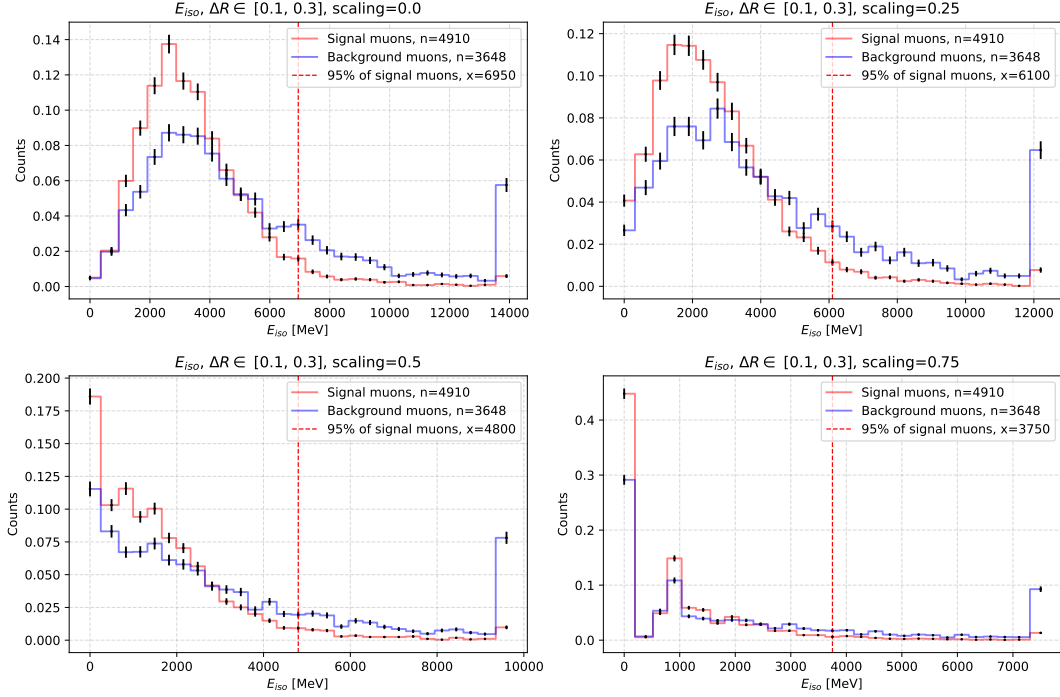


Figure 3.10.: Isolation energy histograms with **noise cuts scaled down** by a *scaling factor*

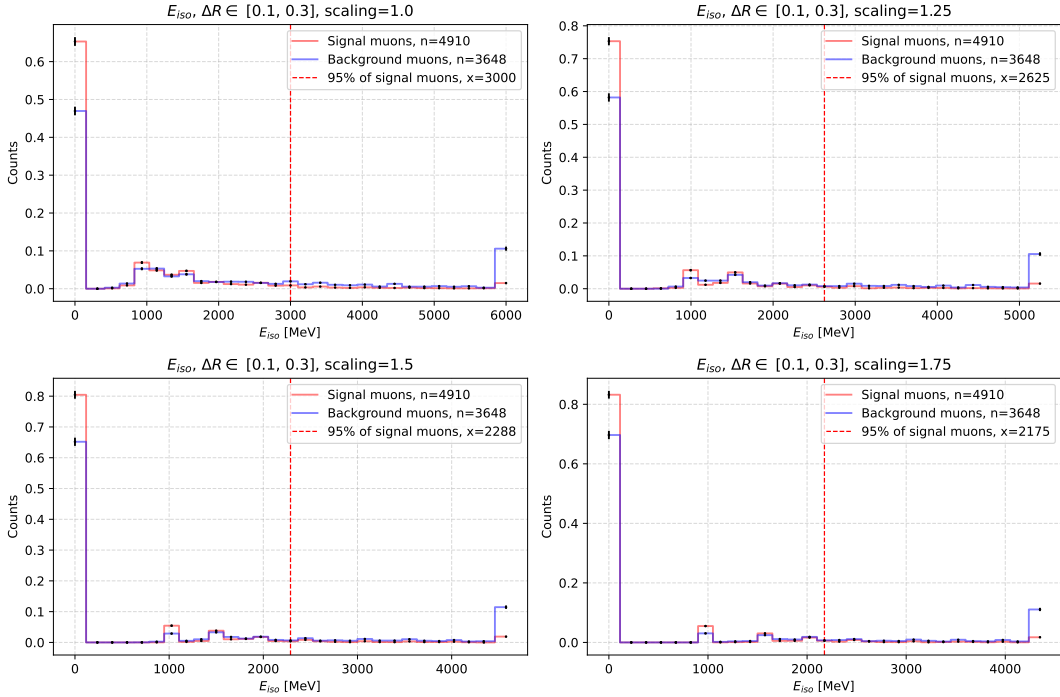


Figure 3.11.: Isolation energy histograms with **noise cuts scaled up** by a *scaling factor*

3. Methodology and Results

3.2.2. Isolation ratios

To help discriminate signal from background data, *isolation ratios* —computed by dividing each muon’s isolation energy by its transverse momentum— have been considered. These quantities use muon p_T as a discriminating variable, with the goal of obtaining a scale-independent distribution (see Figure 3.12).

These ratios demonstrate improved discrimination compared to raw isolation energies, however, they were ultimately not used, since the aim of this study is to improve online signal-to-background discrimination. Ratios cannot be computed online, because muon p_T is unknown by jFEX at the time the trigger’s decision must be made.

Additionally, the p_T spectra of prompt and non-prompt muons differ significantly. As shown in Figure 3.5, ZeroBias muons typically exhibit lower p_T values, with a pronounced tail extending toward higher p_T . In contrast, signal muons are concentrated around 40 GeV, with the vast majority falling within the 20 GeV to 60 GeV range. Consequently, employing ratios in the analysis could introduce undesirable biases.

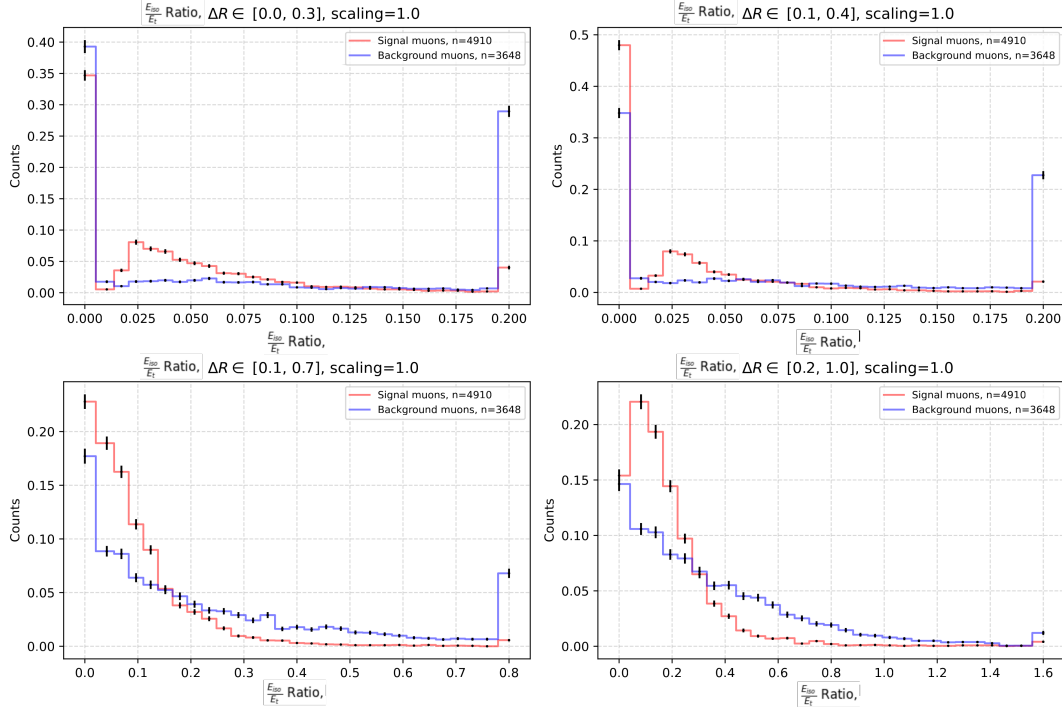


Figure 3.12.: Isolation ratio histograms with different ΔR cones

3.3. ROC curve and Optimization

3.3.1. Receiver Operating Characteristic Curves

A *Receiver Operating Characteristic* (ROC) curve is a measure that illustrates the performance of a signal-background discrimination process, such as distinguishing prompt muons (signal) from those produced by secondary processes (background). The x-axis represents the *False Positive Rate* (FPR), and the y-axis represents the *True Positive Rate* (TPR).

In the context of ATLAS trigger performance, the FPR corresponds to the trigger rate—the rate at which events are accepted by the trigger system—which should ideally be kept low, while the TPR—the fraction of true signal events correctly identified by the trigger—reflects the trigger efficiency, which should be as high as possible.

Figure 3.13 shows how different ΔR cone choices yield varying ROC curves.

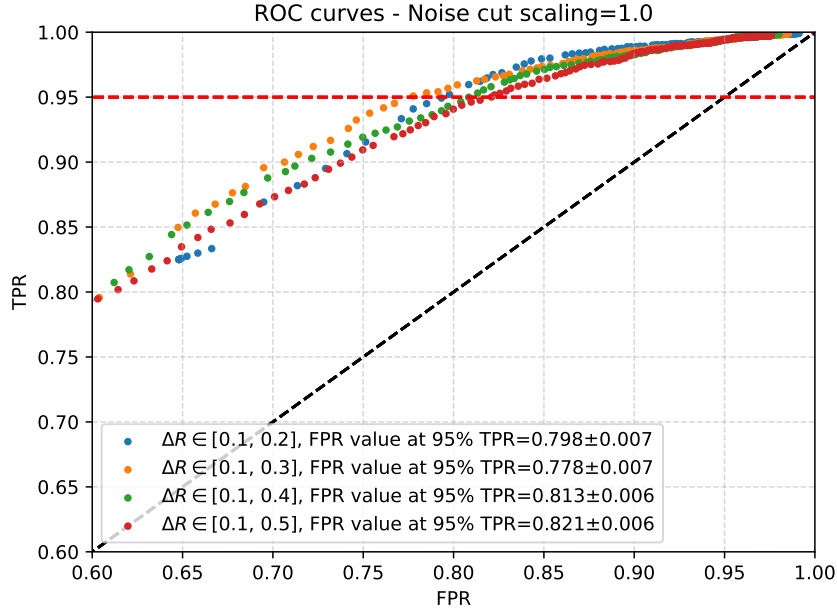


Figure 3.13.: ROC curves for different ΔR cones

In this study, a target efficiency—represented by the horizontal red line—is set at $\text{TPR} = 0.95$. This means that, 95% of the signal muons (i.e., the first 95% of the signal histogram when integrated from left to right) are being selected. While this choice is somewhat arbitrary, it serves as a benchmark reflecting the objective

3. Methodology and Results

of maintaining a high selection efficiency in the analysis. The uncertainty for the $FPR(95\%)$ values was estimated, according to [28] as:

$$\sigma = \sqrt{\frac{\epsilon \cdot (1 - \epsilon)}{n}}$$

where ϵ is the $FPR(95\%)$ value and n is the number of ZeroBias muons considered.

The objective is then to minimize the fraction of background muons selected at this level of signal efficiency. In other words, the goal is to minimize the false positive rate (FPR) when the TPR reaches 0.95. This value will be referred to as $FPR(95\%)$. An optimization process has been performed in order to determine the ΔR cone that better suits this goal.

3.3.2. Isolation energy - p_T relationship

To investigate the dependence of the isolation energy ($E_{T,iso}$) on the muon's transverse momentum (p_T), heatmaps were employed. These plots illustrate the correlation between $E_{T,iso}$ and p_T , as shown in Figure 3.14.

The key observation from these heatmaps is that $E_{T,iso}$ appears largely independent of p_T . The darker regions in the plots simply correspond to an increased density of muons in those p_T intervals, as can be verified by comparing the heatmaps with the p_T spectra in Figure 3.5. Thus, the $E_{T,iso}$ distribution is approximately uniform across the p_T range, reflecting the underlying muon p_T spectrum rather than any intrinsic correlation.

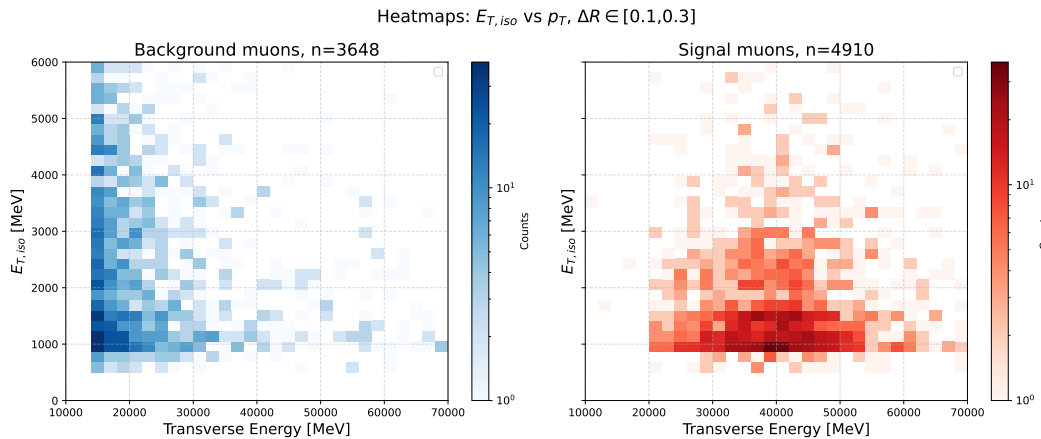


Figure 3.14.: $E_{T,iso}$ vs muon p_T heatmaps, for Background and Signal muons.

3.3.3. Noise cuts dependency

As mentioned in 3.2.1, calorimeter noise cuts are applied to suppress noise and achieve cleaner isolation. Different *scaling factors* were used to linearly increase or decrease the noise cuts in order to study their impact on isolation energies.

As shown in 3.10 and 3.11, isolation energies generally decrease with increasing noise cuts, as more calorimeter towers are classified as noise, and therefore set to 0. However, the FPR(95%) values are not significantly affected, as can be seen in 3.15 and 3.16. This can be explained by the fact that the noise cuts affect both the signal and background distributions in a similar way, and therefore do not introduce additional discrimination between them.

For the final results, the unmodified noise cuts —corresponding to a scaling factor of 1.0— were chosen, as they lead to the lowest FPR(95%) value.

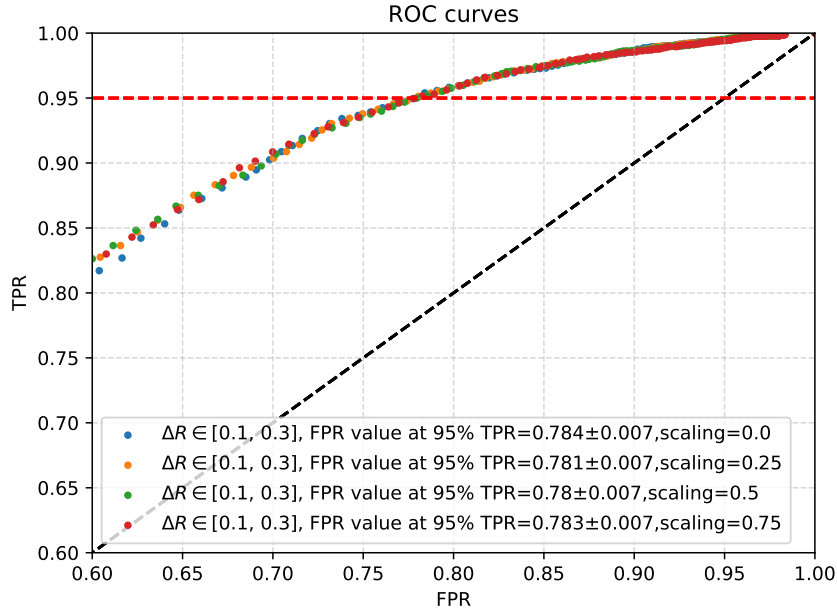


Figure 3.15.: ROC curves with **noise cuts scaled down**

3. Methodology and Results

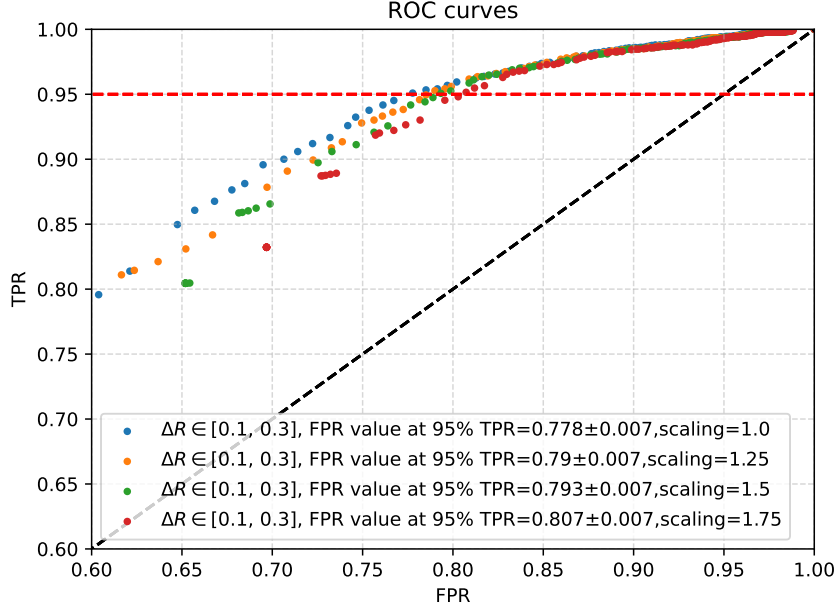


Figure 3.16.: ROC curves with **noise cuts scaled up**

3.3.4. TopoEtCone heatmaps

TopoEtCones are a more sophisticated version of isolation energies compared to those used in this study. These quantities —computed using the full detector granularity— are too computationally expensive to calculate in real time during data taking. The isolation energies used in this study —obtained using coarser granularity— represent an approximate version of the *TopoEtCones*, allowing for computation at the full LHC event rate of 40 MHz.

In this context, the isolation energies were compared with the provided *TopoEtCones* as a sanity check. Figures 3.17, 3.18, 3.19, 3.20, 3.21, and 3.22 show the correlation between them. The labels *Cone20*, *Cone30*, and *Cone40* correspond to ΔR windows of 0.2, 0.3, and 0.4, respectively.

It is important to note that solid cones (3.17, 3.18, 3.19) yield a stronger diagonal correlation, whereas removing the center of the cone leads to a steeper trend (3.20, 3.21, 3.22). This behavior can be explained by the fact that the energy associated with the muon is removed during this process, effectively reducing the total isolation energy compared to the *TopoEtCones*.

3.3. ROC curve and Optimization

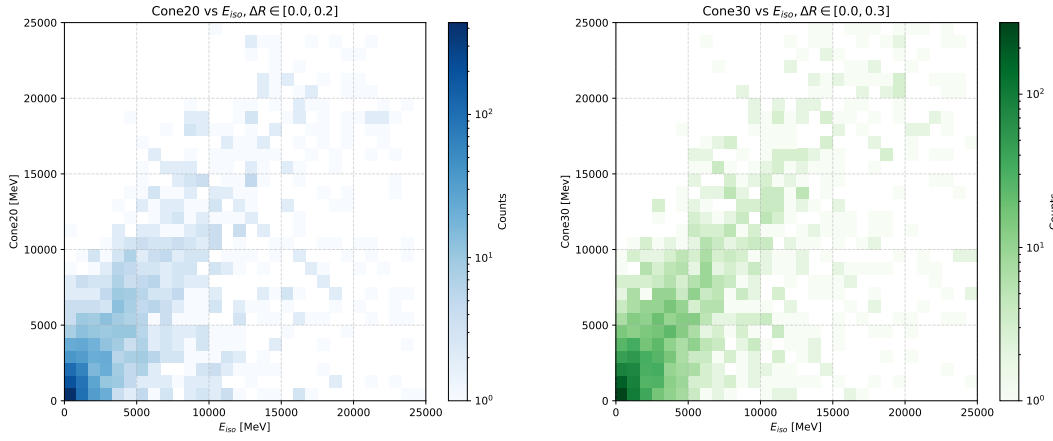


Figure 3.17.: TopoEtCone20 compared to **Figure 3.18.:** TopoEtCone30 compared to $\Delta R \in [0.0, 0.2]$ isolation $\Delta R \in [0.0, 0.3]$ isolation

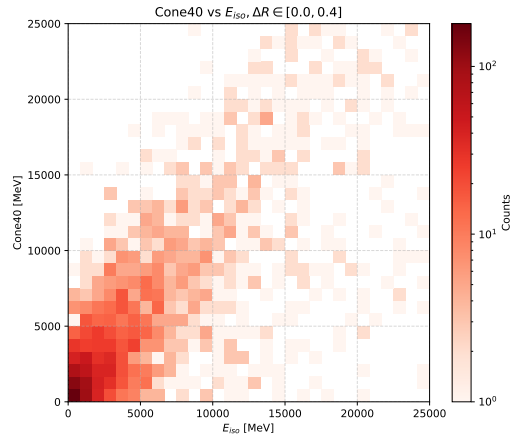


Figure 3.19.: TopoEtCone40 compared to $\Delta R \in [0.0, 0.4]$ isolation

3. Methodology and Results

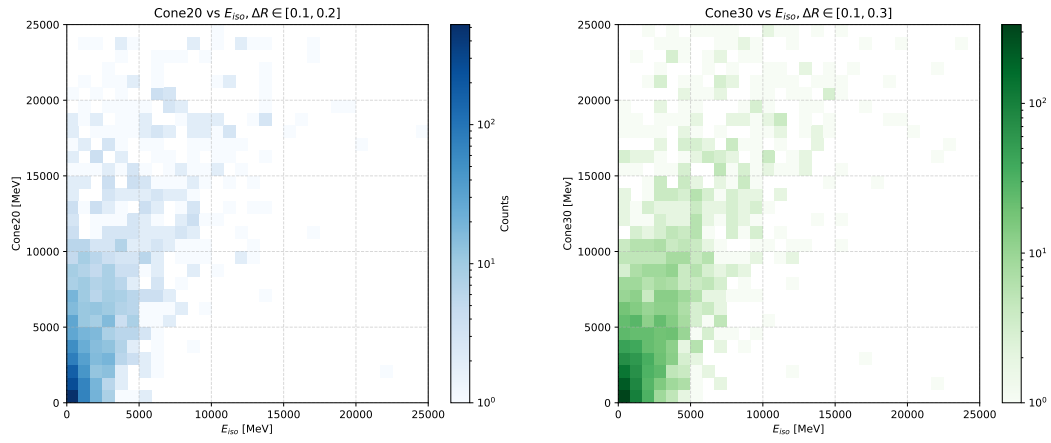


Figure 3.20.: TopoEtCone20 compared to $\Delta R \in [0.1, 0.2]$ isolation **Figure 3.21.:** TopoEtCone30 compared to $\Delta R \in [0.1, 0.3]$ isolation

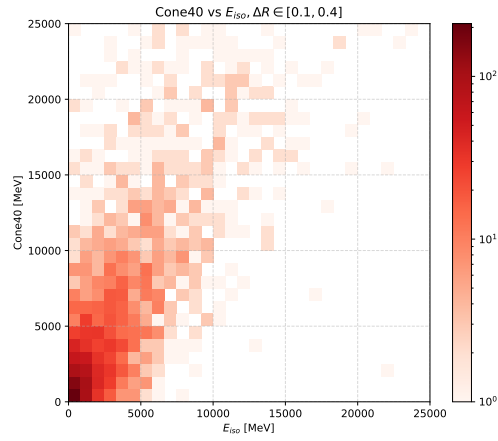


Figure 3.22.: TopoEtCone40 compared to $\Delta R \in [0.1, 0.4]$ isolation

3.3.5. Two-variable optimization

Since two variables—the inner and outer cone radii (denoted as ΔR_{min} and ΔR_{max})—must be optimized simultaneously, a discrete three-dimensional plot has been created. This plot contains a grid of ΔR_{min} and ΔR_{max} values, along with their corresponding FPR(95%) values, as shown in Figure 3.23. Plots for other noise cut scalings are attached in A.1.4. The main conclusions that can be drawn from this plot are:

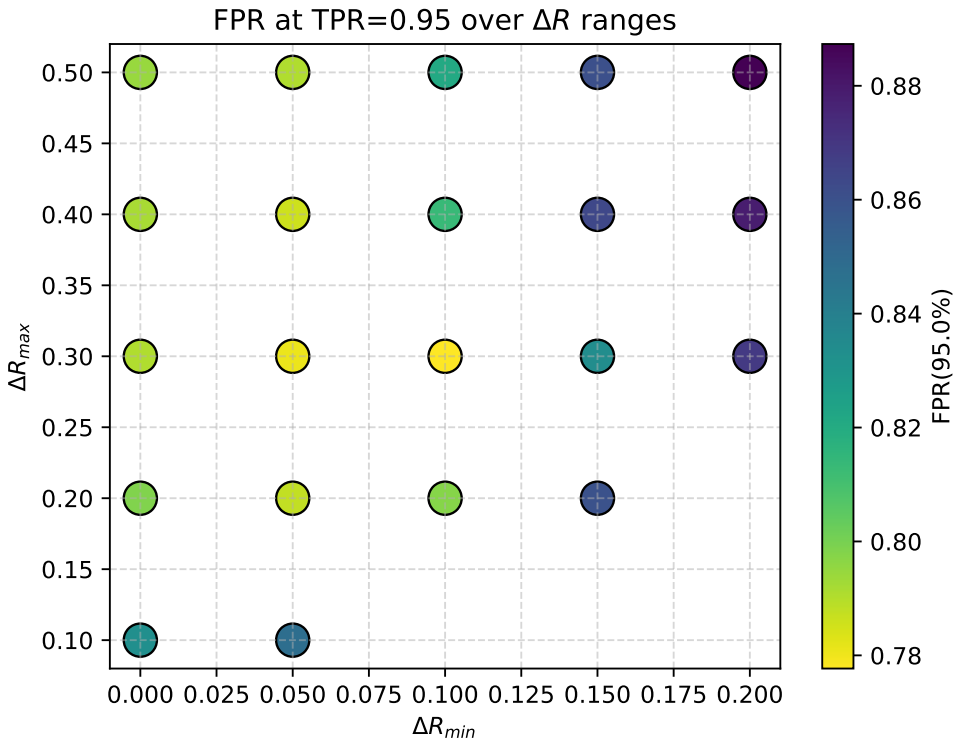


Figure 3.23.: 3D plot, X and Y axis display inner and outer cone choices, respectively, while color of the points indicates the value of FPR(95%)

1. Hollow cones with $\Delta R_{min} \sim 0.1$ generally perform better than solid cones ($\Delta R_{min} = 0$) for prompt muon identification. By removing the inner area, the muon energy, located at the center of the cone, is excluded.

This result may seem counterintuitive, as including the center would add muon energy for prompt muons and both muon and hadron energy for non-prompt muons, which could aid in discrimination. However, the opposite effect is observed. The causes for this effect remain unclear, however, a potential explanation is that the background sample includes “fake” muons, which are misidentified from unrelated hits in the muon system and deposit no energy in

3. Methodology and Results

the calorimeter. As a result, the energy at the center is not informative, since background muons may deposit either less or more energy than signal muons.

On the other hand, if the inner radius is chosen to be too large ($\Delta R_{\min} > 0.1$), a negative impact can be observed. This is likely due to the fact that jets—which are crucial for distinguishing prompt from non-prompt muons—tend to have most of their energy concentrated near the center. When only the outer region is considered, the isolation becomes dominated by noise, reducing the effectiveness of the isolation.

2. Combined with a suitable inner radius, $\Delta R_{\max} \sim 0.3$ yields optimal signal-to-background discrimination. From this, it can be deduced that, for non-prompt muons, a jet’s activity in the calorimeter typically spans a $\Delta\eta \times \Delta\phi$ region of 0.3 or less around the muon’s impact point. Following this reasoning, increasing the outer radius beyond 0.3 would only result in more noise being included in the isolation energies, reducing the effectiveness of the discrimination.

4. Summary and Outlook

4.1. Summary and Conclusions

The ATLAS detector is capable of reconstructing particle collision events with high accuracy and precision. In the current search for new physics, interest has increasingly shifted toward events with lower production cross sections, such as those involving weak decays. To efficiently record such rare phenomena, the Trigger System must determine—within a few microseconds—whether an event exhibits characteristics that justify recording and further processing it. In this context, the Muon Trigger System is particularly relevant, as the presence of muons often signals relatively rare processes, such as $Z \rightarrow \mu^+\mu^-$ decays 2.4.

In this thesis, a novel approach has been explored to optimize the discrimination of prompt muons from muons originating in hadron decays. By employing muon isolation 3 and performing a scan over a wide range of ΔR cones 3.3.5, optimal discrimination was found for a $\Delta R \in [0.1, 0.3]$ cone 4.1. A FPR(95%) of 0.778 ± 0.07 was achieved 4.2. This corresponds to a $\sim 22\%$ reduction in terms of trigger rate, with an efficiency cost of only 5%.

As a conclusion, this proof-of-concept study has produced promising results, motivating further research and development in the quest for new physics discoveries.

4.2. Future work and improvements

This study concludes with several open questions that require careful consideration in future work. To begin with, the results presented here are based on a simplified study aimed at demonstrating the feasibility of the proposed approach. However, it remains unclear how this method could be integrated into the actual Muon Trigger System, or what complexities might arise when attempting to reproduce these results in a real-world environment. Additionally, the samples used in this study did not include low- p_T muons; therefore, no conclusions can be drawn regarding the behavior of the method in this regime. Finally, while the obtained ΔR cones have proven optimal for discriminating prompt muons from Z boson decays, other relevant processes—such as $W \rightarrow \mu\nu$ decays—may exhibit different characteristics that require different ΔR configurations for optimal performance.

4. Summary and Outlook

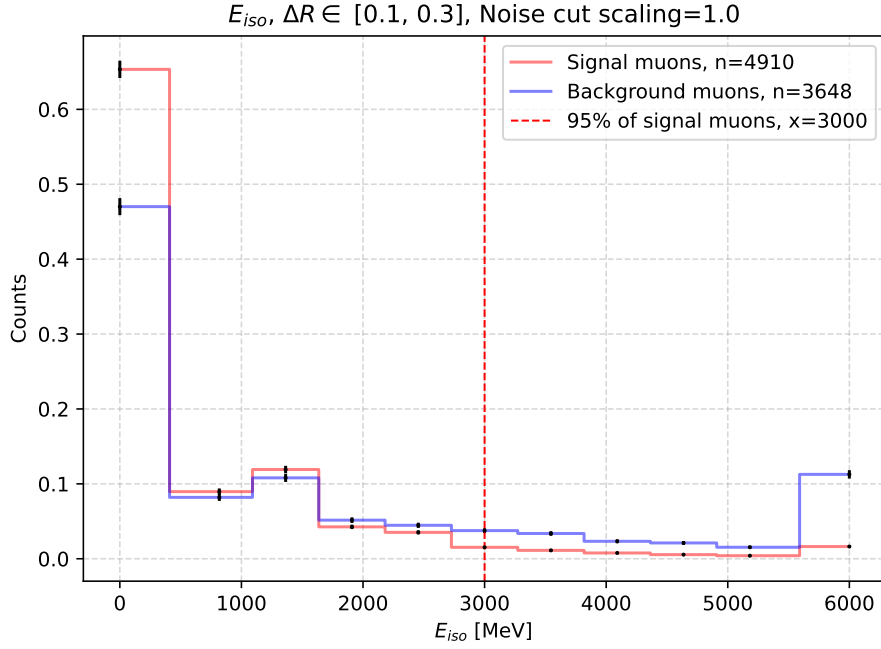


Figure 4.1.: Isolation energy histogram of the **best configuration**

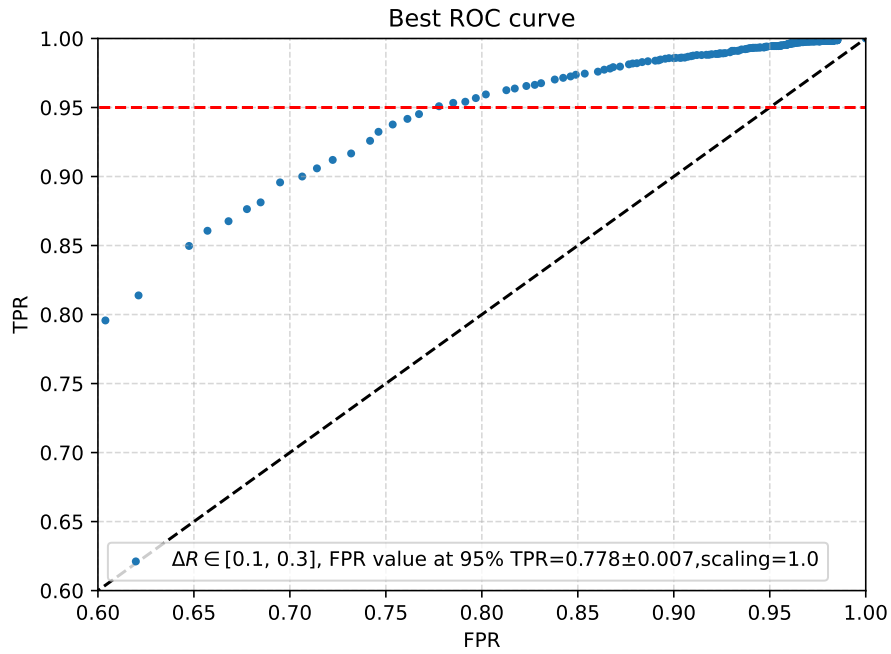


Figure 4.2.: ROC curve of the **best configuration**

A. Appendix

A.1. Tables and References

A.1.1. Invariant mass formulas [18]

$$\begin{array}{lll}
p_{x,1} = p_{t,1} \cdot \cos(\phi_1) & p_{x,2} = p_{t,2} \cdot \cos(\phi_2) & p_x = p_{x,1} + p_{x,2} \\
p_{y,1} = p_{t,1} \cdot \sin(\phi_1) & p_{y,2} = p_{t,2} \cdot \sin(\phi_2) & p_y = p_{y,1} + p_{y,2} \\
p_{z,1} = p_{t,1} \cdot \sinh(\eta_1) & p_{z,2} = p_{t,2} \cdot \sinh(\eta_2) & p_z = p_{z,1} + p_{z,2} \\
E_1 = p_{t,1} \cdot \cosh(\eta_1) & E_2 = p_{t,2} \cdot \cosh(\eta_2) & E = E_1 + E_2
\end{array}$$

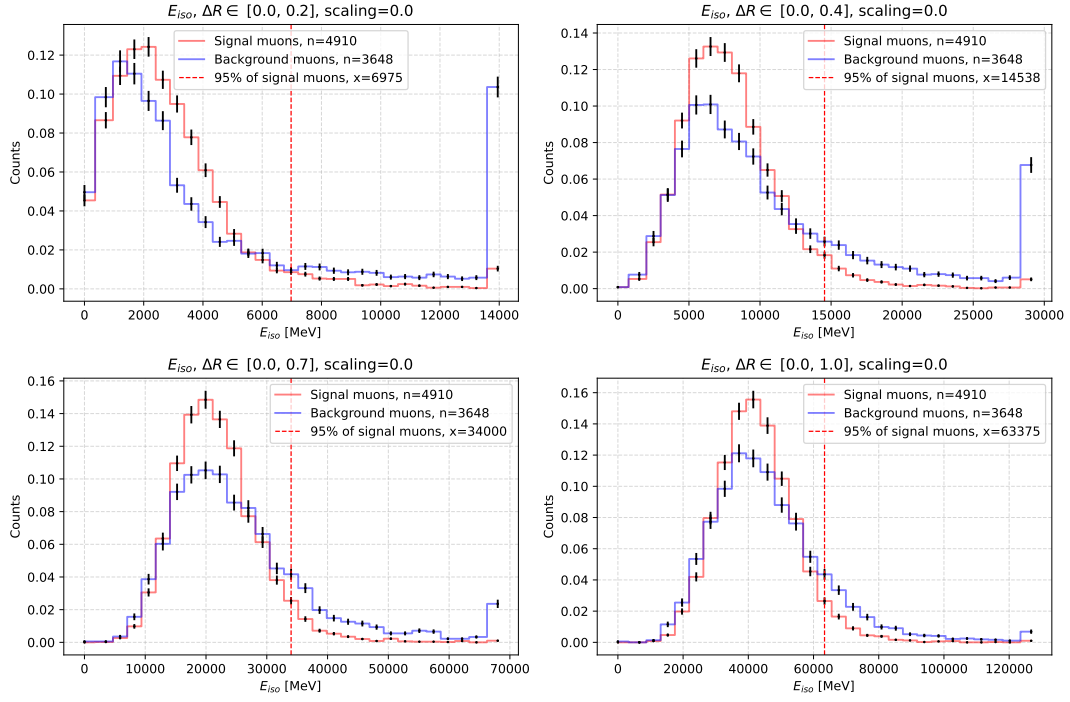
$$m_{\text{inv}}^2 = E^2 - (p_x^2 + p_y^2 + p_z^2)$$

A.1.2. Calorimeter Noise Cuts

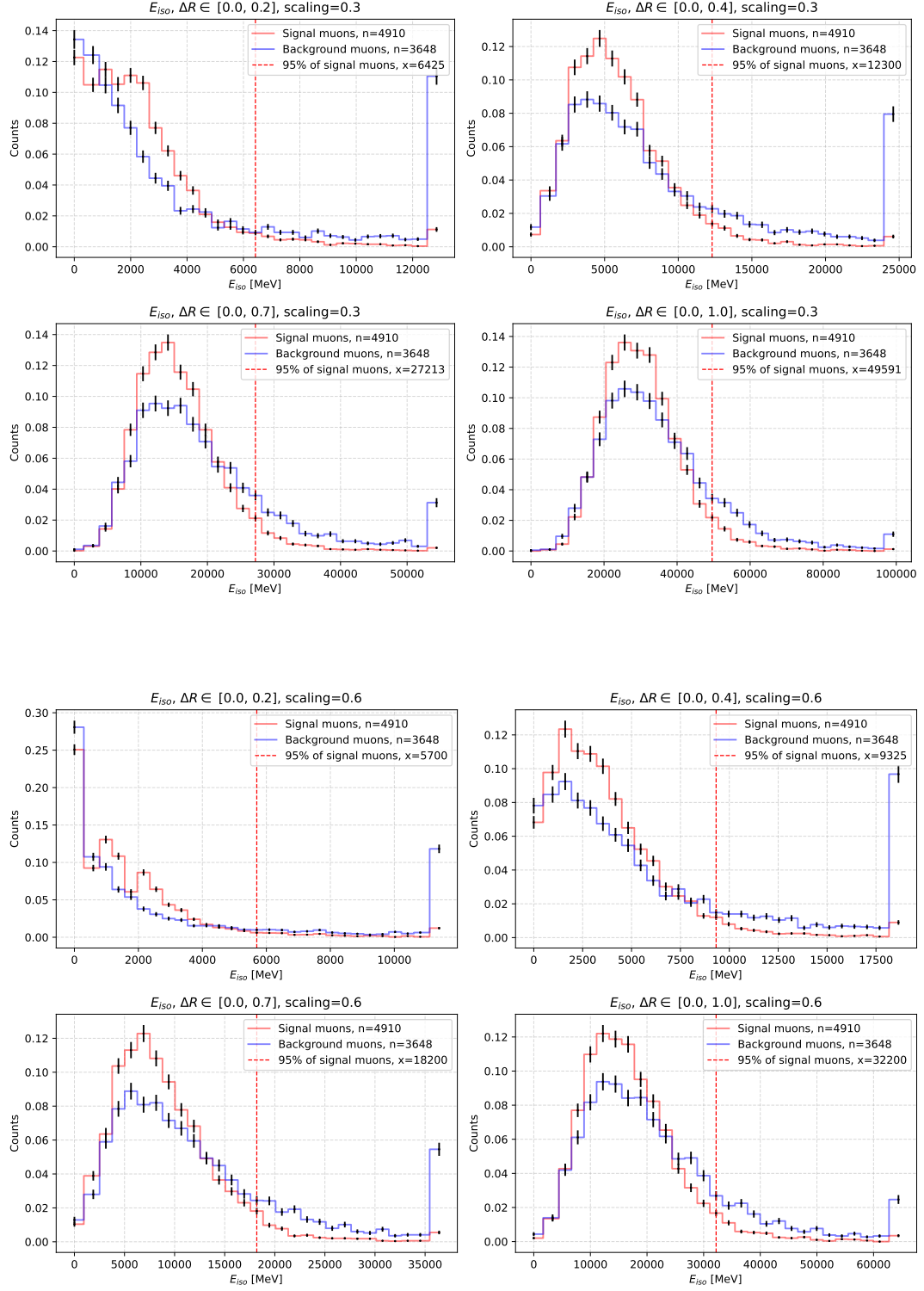
η Interval	EM Noise Cuts [MeV]	HAD Noise Cuts [MeV]
[0, 0.1]	1150	0
[0.1, 0.2]	1150	0
[0.2, 0.3]	1200	0
[0.3, 0.4]	1150	0
[0.4, 0.5]	1100	0
[0.5, 0.6]	1100	0
[0.6, 0.7]	1050	0
[0.7, 0.8]	1050	0
[0.8, 0.9]	1000	0
[0.9, 1.0]	1000	0
[1.0, 1.1]	950	0
[1.1, 1.2]	950	0
[1.2, 1.3]	900	0
[1.3, 1.4]	850	0
[1.4, 1.5]	1300	500
[1.5, 1.6]	1150	950
[1.6, 1.7]	1050	850
[1.7, 1.8]	1000	700
[1.8, 1.9]	1050	750
[1.9, 2.0]	950	700
[2.0, 2.1]	950	650
[2.1, 2.2]	900	650
[2.2, 2.3]	850	600
[2.3, 2.4]	900	550
[2.4, 2.5]	800	1300
[2.5, 2.7]	2150	1250
[2.7, 2.9]	2000	1150
[2.9, 3.1]	1800	350
[3.1, ∞)	1100	0

A. Appendix

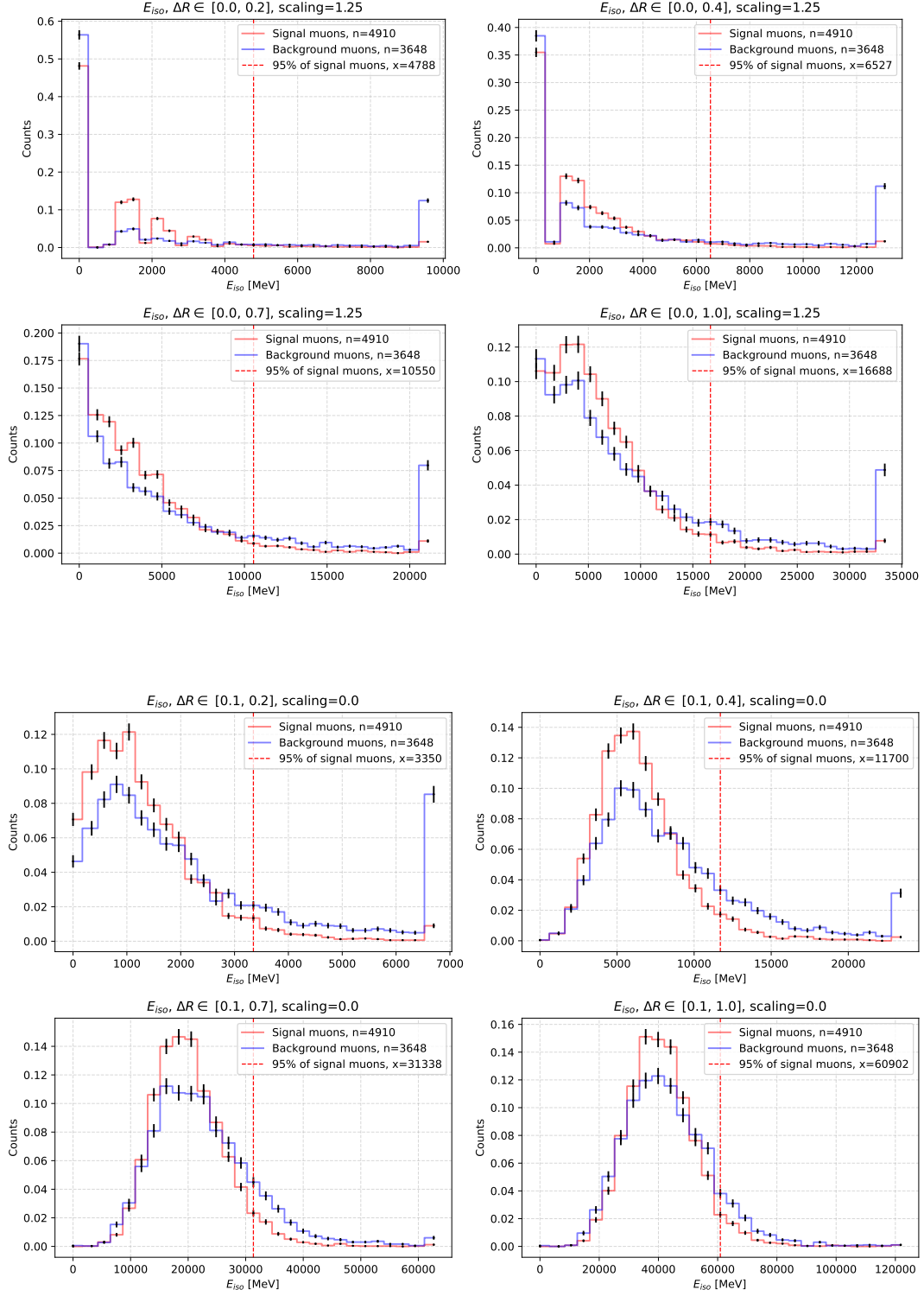
A.1.3. Additional isolation plots



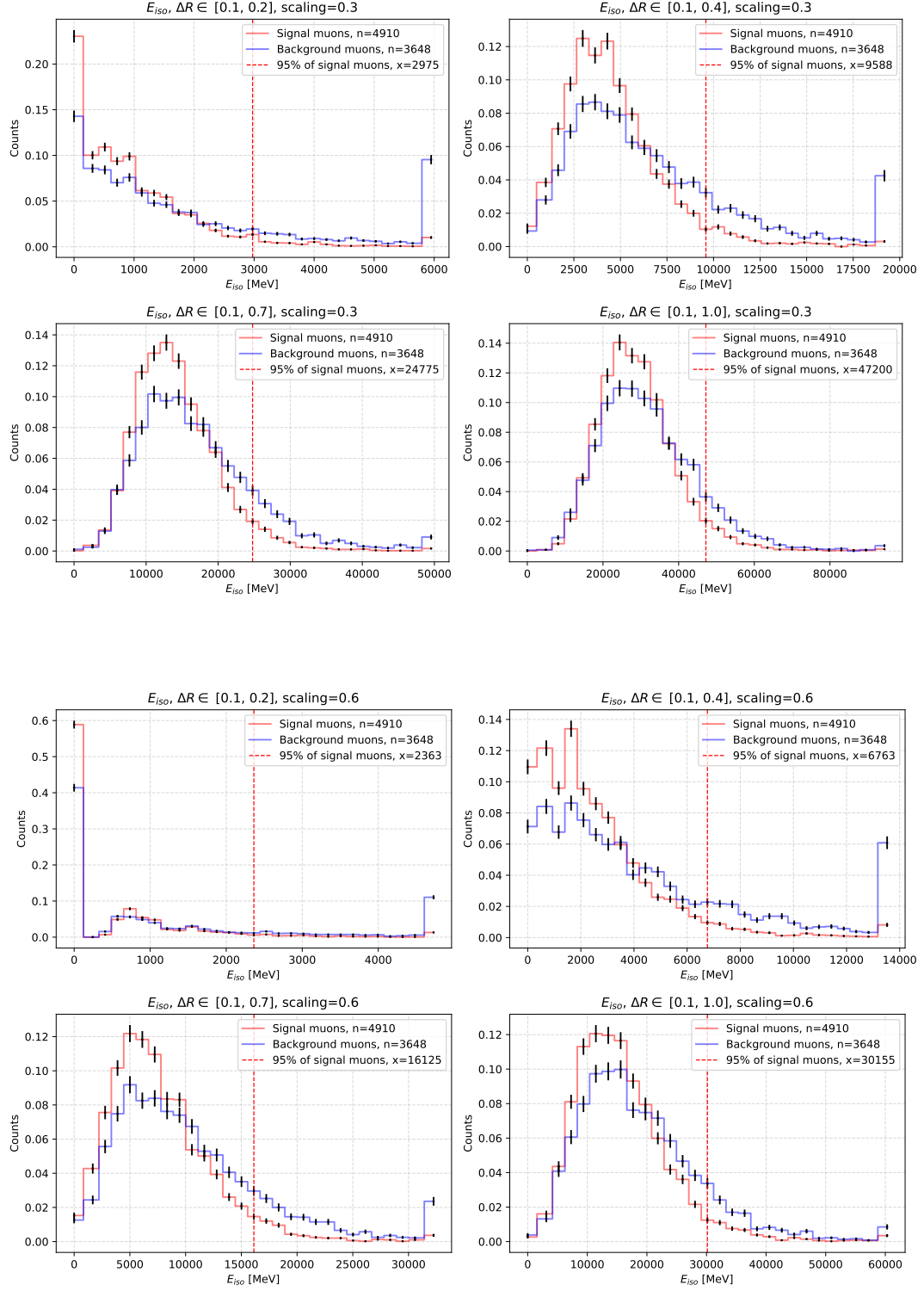
A.1. Tables and References



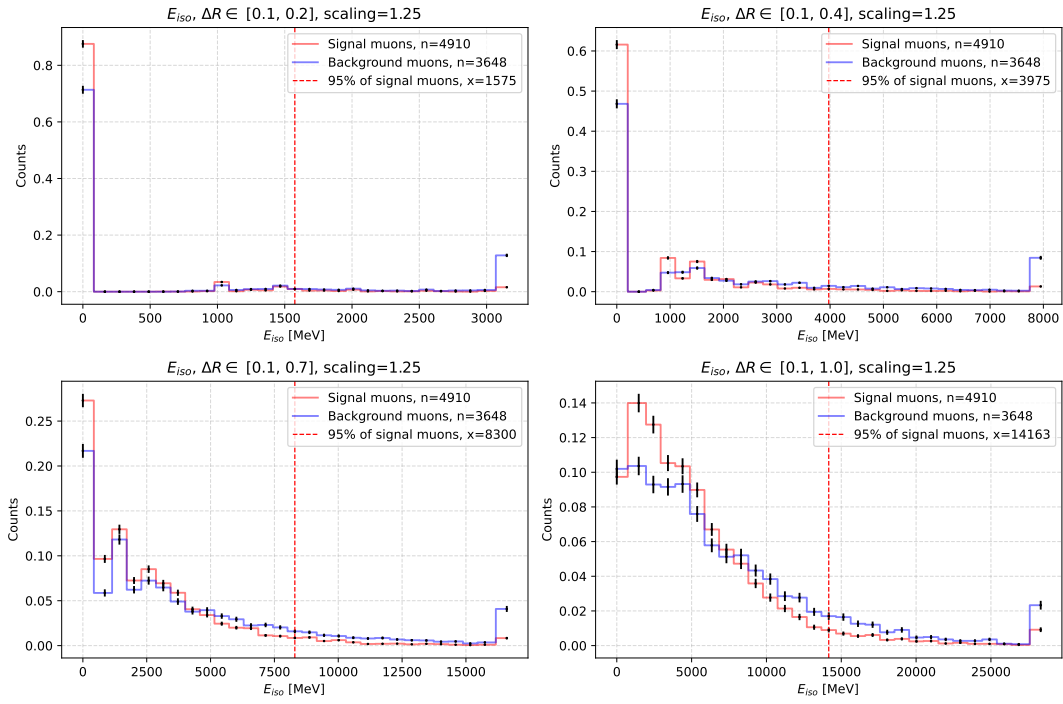
A. Appendix



A.1. Tables and References



A. Appendix



A.1.4. Additional two-variable optimization plots

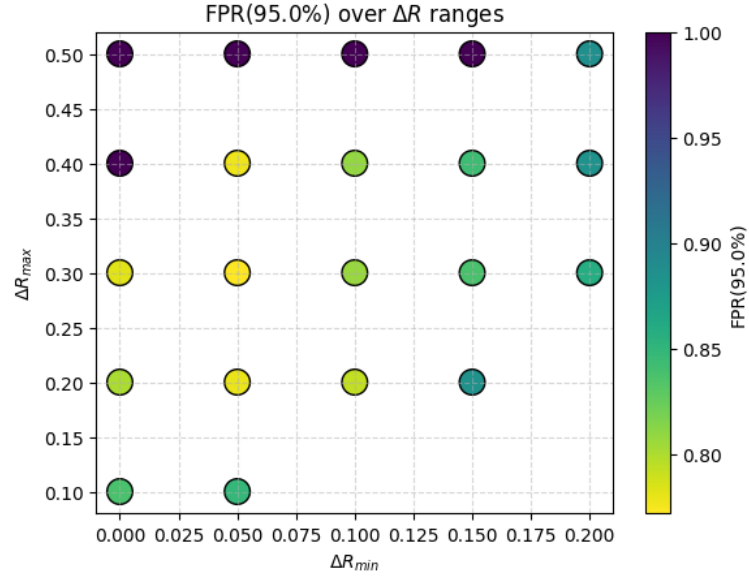


Figure A.1.: Scaling = 0.5

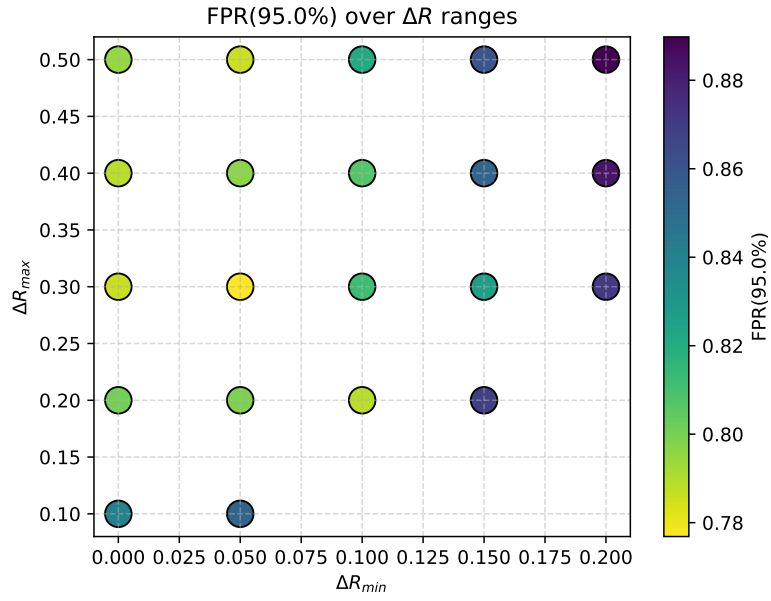


Figure A.2.: Scaling = 0.8

A. Appendix

A.2. Use of AI tools

AI-Tool	Used for	Why	When / Where
ChatGPT	Programming advice and help with detecting grammatical errors or typos.	Great tool for finding bugs in the code, or suggesting improvements. Great for scanning a text and detecting mistakes.	Code and thesis
CursorAI	Faster and more efficient programming	Predicts what you are going to type, and saves a lot of time.	Code

A.3. Acknowledgements

Huge thanks to Ralf Gugel, Moritz Hespig, and Niklas Schmitt for investing their valuable time in my learning, and for their guidance, support, and patience throughout the development of this thesis.

Bibliography

- [1] National Institute of Standards and Technology, Electron Magnetic Moment <https://physics.nist.gov/cgi-bin/cuu/Value?muem>
- [2] L. Evans & P. Bryant, The CERN Large Hadron Collider: Accelerator and Experiments, https://jinst.sissa.it/LHC/LHCmachine/2008_JINST_3_S08001.pdf
- [3] CMS collaboration, Observation of a new boson at a mass of 125 GeV with the CMS experiment at the LHC, <https://arxiv.org/abs/1207.7235>
- [4] ATLAS Collaboration, “Observation of a new particle in the search for the Standard Model Higgs boson with the ATLAS detector at the LHC,” Phys. Lett. B **716** (2012) 1-29, doi:10.1016/j.physletb.2012.08.020, arXiv:1207.7214 [hep-ex].
- [5] European Organization for Nuclear Research (CERN), ATLAS computing: Technical design report, CERN-LHCC-2005-022, 2010. [Online]. Available: <https://cds.cern.ch/record/1384803>
- [6] W. Panduro Vazquez and the ATLAS Collaboration, *The ATLAS Data Acquisition System in LHC Run 2*, Journal of Physics: Conference Series, vol. 898, 032017, 2017. doi: 10.1088/1742-6596/898/3/032017.
- [7] I. Béjar Alonso, O. Brüning, P. Fessia, M. Lamont, L. Rossi, L. Taviani, M. Zerlauth (Eds.), *High-Luminosity Large Hadron Collider (HL-LHC): Technical Design Report*, CERN Yellow Reports: Monographs, Vol. 10 (2020), <https://doi.org/10.23731/CYRM-2020-0010>.
- [8] A. Purcell, Go on a particle quest at the first CERN webfest. Bulletin Issue, BUL- NA-2012-269, August 2012. <http://cds.cern.ch/record/1473657>
- [9] The ATLAS collaboration, A Description of the Detector Configuration for Run 3, <https://arxiv.org/pdf/2305.16623>
- [10] L. Evans & P. Bryant, LHC Machine, <https://iopscience.iop.org/article/10.1088/1748-0221/3/08/S08001/pdf>
- [11] CERN, The accelerator complex, <https://home.cern/science/accelerators/accelerator-complex>
- [12] ATLAS, ATLAS Schematics, <https://atlas.cern/Resources/Schematics>
- [13] ATLAS, Detector & Technology, <https://atlas.cern/Discover/Detector>
- [14] ATLAS, Trigger and Data Acquisition, <https://atlas.cern/Discover/Detector/Trigger-DAQ>
- [15] The ATLAS collaboration, The ATLAS trigger system for LHC Run 3 and trigger performance in 2022, <https://arxiv.org/abs/2401.06630>
- [16] Buttinger W, The ATLAS Level-1 Trigger System, <https://cds.cern.ch/record/1456546>
- [17] Claudia Merlassino, The ATLAS Trigger System, <https://cds.cern.ch/record/2921106>
- [18] Particle Data Group, Kinematics, <https://pdg.lbl.gov/2025/reviews/rpp2024-rev-kinematics.pdf>

Bibliography

- [19] ATLAS Collaboration, Standard Model Summary Plots June 2024, <https://atlas.web.cern.ch/Atlas/GROUPS/PHYSICS/PUBNOTES/ATL-PHYS-PUB-2024-011/>
- [20] R. Placakyte, Parton Distribution Functions, arXiv:1111.5452 [hep-ph], 2011, <https://arxiv.org/abs/1111.5452>
- [21] Particle Data Group, Passage of Particles Through Matter, <https://pdg.lbl.gov/2024/reviews/rpp2024-rev-passage-particles-matter.pdf>
- [22] B. Povh, K. Rith, C. Scholz, F. Zetsche, Particles and Nuclei: An Introduction to the Physical Concepts
- [23] ALICE Collaboration, The ALICE experiment at the CERN LHC, <https://iopscience.iop.org/article/10.1088/1748-0221/3/08/S08002/pdf>
- [24] CMS Collaboration, The CMS experiment at the CERN LHC, <https://iopscience.iop.org/article/10.1088/1748-0221/3/08/S08004/pdf>
- [25] LHCb Collaboration, The LHCb Detector at the LHC, <https://iopscience.iop.org/article/10.1088/1748-0221/3/08/S08005/pdf>
- [26] Particle Data Group, Z boson, <https://pdg.lbl.gov/2020/reviews/rpp2020-rev-z-boson.pdf>
- [27] ATLAS Collaboration, Muon reconstruction performance of the ATLAS detector in proton-proton collision data at $\sqrt{s}=13$ TeV, <https://link.springer.com/article/10.1140/epjc/s10052-016-4120-y>
- [28] Diego Casadei, Estimating the selection efficiency, <https://arxiv.org/pdf/0908.0130>